

1 **A global glacial ocean state estimate constrained by upper-ocean**
2 **temperature proxies**

3 Daniel E. Amrhein^{*†}

4 *MIT-WHOI Joint Program in Oceanography, Cambridge, MA*

5 Carl Wunsch

6 *Harvard University, Cambridge, MA*

7 Olivier Marchal

8 *Woods Hole Oceanographic Institution, Woods Hole, MA*

9 Gael Forget

10 *Massachusetts Institute of Technology, Cambridge, MA*

11 ^{*}*Corresponding author address:* Daniel E. Amrhein, MIT-WHOI Joint Program in Oceanography,
12 Cambridge, MA

13 E-mail: amrhein@uw.edu

14 [†]*Current affiliation:* School of Oceanography and Department of Atmospheric Sciences, University
15 of Washington, Seattle, WA.

ABSTRACT

We use the method of least squares with Lagrange multipliers to fit an ocean general circulation model to the Multiproxy Approach for the Reconstruction of the Glacial Ocean Surface (MARGO) estimates of near sea surface temperature (NSST). Compared to a modern simulation, the resulting global, last-glacial ocean state estimate, which fits the MARGO data within uncertainties in a free-running coupled ocean-sea ice simulation, has global mean NSSTs that are 2°C colder and greater sea ice extent in all seasons in both Northern and Southern Hemispheres. Increased brine rejection by sea ice formation in the Southern Ocean contributes to a stronger abyssal stratification set principally by salinity, qualitatively consistent with pore fluid measurements. The upper cell of the glacial Atlantic overturning circulation is deeper and stronger. Dye release experiments show similar distributions of Southern Ocean source waters in the glacial and modern western Atlantic, suggesting that LGM surface temperature data do not require a major reorganization of abyssal water masses. Outstanding challenges in reconstructing LGM ocean conditions include reducing effects from model drift and finding computationally expedient ways to incorporate abyssal tracers in global circulation inversions. Progress will be aided by the development of coupled ocean-atmosphere-ice inverse modeling approaches, by improving high-latitude model processes that connect the upper and abyssal oceans, and by the collection of additional paleoclimate observations.

³⁷ **1. Introduction**

³⁸ Disagreements among general circulation model (GCM) representations of the Last Glacial
³⁹ Maximum (LGM, ca. 23 - 19 thousand years ago (ka), Mix et al. 2001) and between models
⁴⁰ and LGM paleoceanographic data (Braconnot et al. 2007; Otto-Bliesner et al. 2009; Tao et al.
⁴¹ 2013; Dail and Wunsch 2014) illustrate a gap in our knowledge of Earth's climate during that time
⁴² period. Here we present a global ocean state estimate at the LGM, a dynamically consistent fit
⁴³ of an ocean general circulation model (OGCM) to surface ocean temperature proxies achieved by
⁴⁴ adjusting model initial conditions, boundary conditions, and turbulent transport parameters. This
⁴⁵ work builds on a growing body of literature combining dynamical models with proxy observa-
⁴⁶ tions in order to interpolate between LGM observations, reveal model deficiencies, and quantify
⁴⁷ uncertainties (e.g., Winguth et al. 2000; Kurahashi-Nakamura et al. 2013; Dail and Wunsch 2014;
⁴⁸ Kurahashi-Nakamura et al. 2017).

⁴⁹ Several factors motivate studying the climate of the LGM. First, geologic evidence suggests that
⁵⁰ LGM conditions were a persistent and dramatic excursion from the present-day climate, with large
⁵¹ ice sheets in the Northern Hemisphere, lower sea levels, and a global mean surface air cooling of
⁵² several degrees Celsius (Clark et al. 2012). Second, radiocarbon dating allows measurements to
⁵³ be reliably placed within the LGM time frame. Finally, the LGM is a useful period to study
⁵⁴ the ocean's role in regulating atmospheric carbon dioxide concentrations, with implications for
⁵⁵ understanding modern climate change (Sarmiento and Toggweiler 1984; Siegenthaler and Wenk
⁵⁶ 1984; Brovkin et al. 2007; Shakun et al. 2012) including the sensitivity of climate to atmospheric
⁵⁷ greenhouse gas concentrations (Schmittner et al. 2011; Hargreaves et al. 2012).

⁵⁸ The Multiproxy Approach for the Reconstruction of the Glacial Ocean Surface (MARGO) com-
⁵⁹ pilation of LGM surface ocean temperature estimates (MARGO Project Members 2009) extends

the previous work of GLAMAP (Pflaumann et al. 2003) and CLIMAP (McIntyre et al. 1976) by including more observations from a wider range of temperature proxy types. We refer to these data as representing “near” sea surface temperature (NSST) in recognition of the various depth ranges inhabited by organisms used for temperature reconstructions. Numerous studies have used the MARGO database as a basis for comparison with numerical models, often showing qualitative disagreements on regional scales. Simulations from the Paleoclimate Modeling Intercomparison Projects (PMIP1, PMIP2 and PMIP3) used LGM boundary conditions, including global sea level, orography, greenhouse gases, and Earth’s orbital parameters (Braconnot et al. 2007), in climate models of varying complexity. Hargreaves et al. (2011) found that the inter-model spread of simulated NSSTs in PMIP1 and PMIP2 did not disagree with MARGO data within its uncertainty. However, Dail and Wunsch (2014) found that, when considered individually, five PMIP2 simulations fit MARGO data poorly in the North Atlantic. In the tropical oceans, Otto-Bliesner et al. (2009) found that PMIP2 models had a similar range of global mean NSST decrease to that estimated by MARGO, and that simulated Atlantic cooling was larger than in the Pacific, also in agreement with the observations, but that zonal gradients of LGM cooling in tropical Pacific near surface waters were less pronounced than in MARGO. Model ensemble averages reported by Braconnot et al. (2007) and individual model results from Tao et al. (2013) show North Atlantic cooling patterns with a zonal gradient opposite that seen in the data. Data errors contributing to these disagreements could arise from chronological errors, representational errors, seasonal biases, and biological proxy effects, to name a few. Model errors potentially include incorrectly specified initial and boundary conditions, errors in numerical solution methods, missing physics, and inaccurate parameterizations of unresolved phenomena (e.g., ocean eddies and clouds).

The Atlantic abyssal circulation may have played an important role in maintaining a climate at the LGM that was different from the modern through its role in transporting and storing heat, bio-

logical nutrients, and carbon. For instance, one interpretation of paleoceanographic data from the Atlantic is that during the LGM, deep water originating from the North Atlantic shoaled and bottom water from the Southern Ocean filled more of the abyss (e.g., Curry et al. 1988; Duplessy et al. 1988; Marchitto et al. 2002; Curry and Oppo 2005; Marchitto and Broecker 2006; Lynch-Stieglitz et al. 2007), possibly coincident with a weakening and shoaling of the upper cell of the Atlantic Meridional Overturning Circulation (AMOC). This scenario is simulated in some, but not all, numerical models. While PMIP2 LGM experiments showed a broad range of strengths and depths of the upper and lower cells of the AMOC (Otto-Bliesner et al. 2007), nearly all PMIP3 simulations show deeper, strong upper-cell AMOC transport at the LGM relative to modern simulations (Muglia and Schmittner 2015). By contrast, simplified ocean models considered by Ferrari et al. (2014) and Jansen and Nadeau (2016) point to a shallower, weaker LGM upper cell. Differences among models may arise from different model architectures, spatial resolution, bathymetry, physical parameterizations, or incomplete model spin-up (Zhang et al. 2013; Marzocchi and Jansen 2017). Finally, estimates of LGM salinity derived from the pore fluids of sediment cores suggest that the global ocean was not only saltier, due to the storage of fresh water in ice sheets, but also more salt-stratified in the abyss (Adkins et al. 2002; Insua et al. 2014). However, Miller et al. (2015) and Wunsch (2016) argue that pore fluid measurements are too few to be uniquely interpretable.

Fitting models to paleoceanographic data can improve our knowledge of model and data shortcomings. Ultimately, this approach can improve our knowledge of the ocean circulation and climate at time intervals like the LGM. Previous efforts include Dail (2012) and Dail and Wunsch (2014) (hereafter DW14), who obtained a state estimate of the LGM Atlantic Ocean by fitting an OGCM to Atlantic MARGO data, and Kurahashi-Nakamura et al. (2017) (hereafter KN17), who fit an OGCM to the global annual-mean MARGO data as well as oxygen and carbon isotope

¹⁰⁸ ratios in the Atlantic Ocean. Other efforts to constrain the abyssal circulation during the LGM
¹⁰⁹ by combining models and proxy data include LeGrand and Wunsch (1995); Gebbie and Huybers
¹¹⁰ (2006); Marchal and Curry (2008); Burke et al. (2011); Gebbie (2014), and Gebbie et al. (2016).
¹¹¹ A common conclusion of these studies is the difficulty in determining past circulations uniquely
¹¹² because of the sparsity and noisiness of paleoceanographic measurements.

¹¹³ Here we present a new fit of an OGCM to the MARGO dataset of global, seasonal gridded
¹¹⁴ NSST observations. This work expands upon Dail and Wunsch (2014) by using (i) a global do-
¹¹⁵ main, (ii) a longer model integration, and (iii) atmospheric forcings derived in part from a coupled
¹¹⁶ ocean-atmosphere model LGM simulation. Differences from KN17 include (i) the use of higher
¹¹⁷ spatial resolution both horizontally and vertically (2 vs 3 degrees and 50 vs 15 vertical levels,
¹¹⁸ respectively), and (ii) the inclusion of seasonal MARGO data. Unlike KN17, we exclude oxygen
¹¹⁹ and carbon isotope data in the deep ocean from the state estimate, as simulation durations required
¹²⁰ to equilibrate abyssal tracer distributions (thousands of model years) proved to be too computa-
¹²¹ tionally expensive for our state estimation framework, and fitting incompletely equilibrated model
¹²² tracers to observations can lead to biased solutions (Dail 2012; Amrhein 2016). Our state estimate
¹²³ is a freely-running primitive equation ocean model simulation that agrees with seasonal MARGO
¹²⁴ data within estimated errors and allows us to analyze approximately equilibrated properties of the
¹²⁵ ocean circulation, including in the abyss. A comparison of LGM state estimates in the Discussion
¹²⁶ provides insights into their uncertainties and sensitivities to different state estimation approaches.

127 **2. Materials and Methods**

128 *a. LGM NSST data*

129 NSST data and uncertainties are from the $5^\circ \times 5^\circ$ MARGO gridded products (MARGO Project
130 Members 2009) constructed from microfossil and chemical measurements in ocean sediment cores
131 representing the time interval 23-19 kyr BP. The MARGO compilation includes transfer function
132 approaches – which match past abundances of planktonic foraminifera, diatoms, dinoflagellate
133 cysts, or radiolarians to modern analogues – and chemical thermometers based on alkenone in-
134 dices and planktonic foraminiferal Mg/Ca. Gridded values are weighted means of proxy values,
135 with weights based on data type, numbers of observations available during the time period, and
136 calibration and instrumental errors. Three separate gridded MARGO products represent annual,
137 January-February-March (JFM), and July-August-September (JAS) mean conditions. The spatial
138 density of the gridded data is highest in tropical regions and at high northern latitudes, especially
139 in the northern North Atlantic and Arctic Oceans. Data from the Southern Ocean are restricted to
140 austral summer due to the limited seasonal representativeness of diatom assemblages, which make
141 up most available observations in that region.

142 *b. The MITgcm*

143 The OGCM we fit to the MARGO data is the MITgcm, an evolved form of that described by
144 Marshall et al. (1997) and Adcroft et al. (2004) that simulates the ocean circulation under hydro-
145 static and Boussinesq approximations. The model is a lower-resolution configuration of the ECCO
146 version 4 release 2 modern state estimation setup (Forget et al. 2015a, hereafter ECCO), with 2°
147 horizontal resolution telescoping to higher resolution at the equator and the poles and 50 vertical
148 levels with thicknesses ranging from 10 m at the surface to 456 m at 5900 m. The MITgcm is cou-

pled to a viscous plastic dynamic-thermodynamic sea ice model (Losch et al. 2010) subject to the same atmospheric forcing as the ocean model. Air-sea fluxes of heat, fresh water, and momentum are computed using the bulk formulae of Large and Yeager (2004). Global mean freshwater fluxes through the sea surface are compensated at every time step by adding or subtracting a uniform freshwater flux correction that prevents drifts in global mean ocean salinity. Ocean vertical mixing is parameterized using the turbulent closure scheme of Gaspar et al. (1990). Isopycnal diffusivity is treated using the Redi (1982) scheme, and unresolved eddy advection is parameterized using the method of Gent and McWilliams (1990). Following Bugnion and Hill (2006) and Dail (2012) we use accelerated time stepping (Bryan 1984), with a tracer time step of 12 hours and a momentum time step of 20 minutes.

Model bathymetry for the LGM was constructed by smoothing and subsampling modern water depth estimates (Smith and Sandwell 1997) and adding the LGM minus modern bathymetry anomaly reconstructed by Peltier (2004), which has a median LGM sea level of approximately 130 meters below present. A seasonal cycle of runoff is derived from Fekete et al. (2002), with runoff on the European continent between 50° and 72°N rerouted to the latitude of the English Channel, reflecting the reconstruction of Alkama et al. (2006). Sea ice and snow albedos were reduced by roughly 30% from ECCO values to prevent unrealistic sea ice growth in the LGM state estimate.

166 *c. State estimation procedure*

167 Procedures for obtaining data-constrained ocean state estimates used in this paper are illustrated
168 in the flowchart in Figure 1. We use the method of least squares with Lagrange multipliers (also
169 known as the adjoint method; e.g., Wunsch 2006) to fit the MITgcm to seasonal- and annual-mean
170 MARGO NSST data. In modern oceanography, the relative wealth of observations permits esti-
171 mating the time-varying ocean state (Stammer et al. 2002; Wunsch and Heimbach 2007; Forget

172 et al. 2015a). At the LGM, the sparsity of the data motivates treating them as samples of a “sea-
173 sonally steady” state – a single seasonal cycle that repeats over the interval 23-19 ka. Our goal
174 is to generate an MITgcm simulation under annually repeating atmospheric boundary conditions
175 that both fits the data within their uncertainties and is consistent with a quasi-steady circulation,
176 as defined below. We will denote vectors and matrices by lower- and upper-case bold letters,
177 respectively.

178 The ocean state vector at a time t , $\mathbf{x}(t)$, is a complete list of the variables required to take one
179 model time step – temperature, salinity, velocity, etc. – at all locations of the model grid. An
180 underbar denotes a vector of monthly mean values, e.g. $\underline{\mathbf{x}}$ is a list of all model variable values av-
181 eraged over January, February, etc. The evolution of the MITgcm under seasonally steady forcing
182 can be written as

$$\mathbf{x}(t + \Delta t) = \mathcal{L}(\mathbf{x}(t), \mathbf{q}(t), \underline{\mathbf{u}}), \quad 0 \leq t \leq t_f = M\Delta t \quad (1)$$

183 where \mathcal{L} is a nonlinear operator, Δt is the discrete model time step, M is a positive integer, $\mathbf{q}(t)$ is a
184 vector of model parameters that are not changed in the optimization (e.g., model bathymetry), and
185 $\underline{\mathbf{u}}$ is a vector of adjustable “control” variables (or “controls”) including fields of initial temperature
186 and salinity, turbulent transport parameters, and monthly average atmospheric forcing (Table 1).

187 The state estimate is obtained by iteratively minimizing a cost function with three terms. The
188 first term penalizes misfits between the model and data, the second penalizes large changes to
189 the controls, and the last imposes the dynamical constraints of the model using the Lagrange
190 multipliers. At each iteration, the model is run forward, cost is computed, and the model adjoint
191 is used to estimate the linear sensitivity of the cost function to the controls (Appendix A). Then
192 control adjustments are made, the model is run again, costs are recomputed, and the cycle repeats.
193 The data cost function term is calculated as the sum of squared model-data misfits averaged over
194 the last 20 years of a 100-year-long forward simulation, weighted inversely by estimated data error

195 provided as part of the MARGO dataset. The 100-year adjoint integration period is long enough
196 to bring much of the surface ocean into near-equilibrium with changes in seasonal atmospheric
197 conditions but too short to equilibrate deep ocean tracers (Wunsch and Heimbach 2008). Our
198 results could be biased against dynamical mechanisms that could reduce model-data misfits on
199 time scales longer than a century.

200 While we assume LGM observations represent a seasonally steady cycle, we do not require
201 exact seasonal steadiness in our state estimate. This is a practical choice, as finding seasonally
202 steady circulations that fit the data requires simulations of thousands of years at each iteration
203 of the model adjoint, which is computationally prohibitive. A broader rationale is that requiring
204 a seasonally steady circulation excludes states with variability at periods between one year and
205 the duration of the LGM. Such variability is a major feature of the modern climate, and has been
206 shown to influence the time-mean ocean state (e.g., Guilyardi 2006). While the data do not have
207 the power to resolve this variability, excluding it may bias reconstructions of the LGM.

208 Our state estimate is the last year from a 5000-year-long model simulation that is run using con-
209 trol adjustments that are derived to fit the model to the data in 100-year-long adjoint simulations.
210 Analyzing the state at the end of a long simulation allows the abyssal ocean approximately to
211 equilibrate to changes derived to fit surface observations (MARGO). We define the state estimate
212 to be sufficiently steady if the simulation it is taken from fits the seasonal data over its 5000-year
213 duration (which has a duration similar to that of the LGM). Because interannual and longer-period
214 variability in our simulation arises mostly from model drift that is monotonic after an initial tran-
215 sient, rather than computing misfits over the entire 5000-year duration, we compute model-data
216 misfits near the beginning and end of the simulation (at model years 80-100 and 4980-5000) and

217 evaluate whether the simulation satisfies the sets of equations

$$\underline{\mathbf{y}} = \mathbf{E}\underline{\mathbf{x}}_{5000} + \underline{\mathbf{n}}_{5000} \quad (2)$$

$$\underline{\mathbf{y}} = \mathbf{E}\underline{\mathbf{x}}_{100} + \underline{\mathbf{n}}_{100}. \quad (3)$$

218 Here $\underline{\mathbf{x}}_{100}$ and $\underline{\mathbf{x}}_{5000}$ are the simulated monthly seasonal cycles averaged over 20 years preceding
219 the 100th and 5000th years of the simulation, respectively; \mathbf{E} is a matrix relating MARGO NSSTs,
220 $\underline{\mathbf{y}}$, to $\underline{\mathbf{x}}_{100}$ and $\underline{\mathbf{x}}_{5000}$; and $\underline{\mathbf{n}}_{100}$ and $\underline{\mathbf{n}}_{5000}$ are residuals to the model fit that should be consistent with
221 magnitudes and patterns of observational errors.

222 *d. Control variables, error covariances, and a first-guess solution*

223 State estimation requires specifying first-guess control values to which adjustments are added
224 to fit the data. First guesses of atmospheric controls (Table 1) are the sums of modern ECCO
225 fields (Forget et al. 2015a) and LGM minus pre-industrial anomalies computed in the Community
226 Climate System Model, version 4 (CCSM4; these anomalies are referred to below as Δ CCSM4).
227 We choose to add Δ CCSM4 to modern ECCO fields rather than simply using CCSM4 LGM fields
228 in an effort to mitigate potential biases from CCSM4. ECCO ocean salinity and temperature are
229 taken from the year 2007 based on the availability of modern observations. The fact that 2007
230 was an El Niño year may contribute to zonal Pacific temperature gradients observed in patterns of
231 model drift. More generally, though we do not attempt to estimate it here, sensitivity to choices of
232 first-guess conditions is an important contributor to solution uncertainty and should be prioritized
233 in future uncertainty quantification studies. The CCSM4 consists of coupled ocean, atmosphere,
234 land, and sea ice models with nominal 1° horizontal resolution. The pre-industrial (PI) CCSM4
235 simulation (Gent et al. 2011) follows protocols for the fifth phase of the Climate Model Inter-
236 comparison Project (CMIP5), while the LGM CCSM4 simulation (Brady et al. 2013) follows

237 PMIP3 protocols, using LGM orbital parameters, greenhouse gas concentrations estimated from
238 ice cores, modified orography due to Northern Hemisphere ice sheets, and reduced global sea
239 level. Δ CCSM4 wind stress anomalies reflect orographic changes due to the presence of Northern
240 Hemisphere ice sheets (Brady et al. (2013); Figure 2a). Surface air temperatures are everywhere
241 reduced in the CCSM4 LGM simulation relative to the pre-industrial, with especially pronounced
242 cooling in the subpolar North Atlantic, Southern, and North Pacific Oceans (Figure 2e). Down-
243 welling longwave radiation (Figure 2k) and humidity (Figure 2i) are also uniformly lower at the
244 LGM, likely reflecting changes in atmospheric heat content and the reduced capacity of colder
245 air to hold moisture. Anomalies of precipitation (Figure 2g) and shortwave downwelling radiation
246 (Figure 2m) show more complex patterns, possibly reflecting differences in simulated atmospheric
247 circulation and cloud distributions as well as changes in Earth's orbital configuration. In many re-
248 gions these anomalies have the same order of magnitude as time-mean modern values.

249 The state estimation procedure also requires first guesses of the glacial distributions of ocean
250 temperature and salinity, which are taken from a 5,000-year-long simulation of the MITgcm LGM
251 configuration (referred to as PRIOR) forced by the first-guess atmospheric conditions (Table 1).
252 Initial conditions of temperature and salinity used for this simulation are from the ECCO modern
253 ocean state plus an additional 1.1 salinity at every model grid box, based on the global mean
254 salinity change estimated at the LGM from pore fluid data (Adkins et al. 2002).

255 Finally, we must assume values for the standard deviations, σ , of the uncertainties in our choices
256 of first-guess control variables. Following DW14, σ for shortwave and longwave downwelling
257 radiation, humidity, and precipitation are twice those used in ECCO, and σ for surface atmospheric
258 temperature is four times that in ECCO. Wind stress σ is set to 0.1 Pa, reflecting the amplitudes
259 of CCSM4 LGM-PI wind stress changes. For initial salinity, σ is 1 on the practical salinity scale,
260 comparable to the estimated change in ocean mean salinity over the last deglaciation. Errors for

261 turbulent transport parameters are taken from ECCO. We assume that control variable uncertainties
262 do not covary in space or between variables.

263 **3. Results**

264 This section reports results from fitting the MITgcm to MARGO LGM NSST estimates and de-
265 scribes properties of the best-estimate LGM ocean state, referred to below as GLACIAL. We also
266 describe the modern simulation (MODERN) used to compare to GLACIAL. It must be empha-
267 sized that we do not claim that our state estimate is a unique fit to the data; other ocean states may
268 exist that are qualitatively different but fit the data equally as well. In particular, the abyssal ocean
269 appears at best to be weakly constrained by the MARGO data (Kurahashi-Nakamura et al. 2013).

270 *a. Construction of the MODERN simulation and comparison to the modern ocean*

271 The MODERN simulation is generated by a 5000-year integration of the MITgcm configuration
272 used to generate the GLACIAL state estimate, but using modern bathymetry and atmospheric con-
273 ditions (Figure 1). Together with GLACIAL, we use MODERN to illustrate differences between
274 the modern and last glacial ocean – rather than a modern state estimate, or modern observations –
275 because taking the difference between the two time intervals removes many (though not all) of the
276 systematic errors in model absolute values. In particular, after 5000 years of integration, annual-
277 mean surface values (lying in the uppermost grid box, centered on 5 m water depth) of temperature
278 and salinity show regional deviations from modern ECCO state estimate values, which are con-
279 strained by modern observations, of over 4°C and 2, respectively (Figures 3a and 3c). By contrast,
280 annual mean temperature anomalies between GLACIAL and MODERN (Figure 5a) do not show
281 the same regional deviations.

282 While some differences between the MODERN simulation and ECCO may arise from the dis-
283 equilibrium of the modern ocean with modern atmospheric conditions, a reasonable conclusion is
284 that much of the difference arises from model error, particularly the model “drift” that is a com-
285 mon phenomenon in ocean-only models lacking atmosphere-ocean feedbacks (e.g., Griffies et al.
286 2009). In addition to changes in surface values, a notable consequence of the drift is the struc-
287 ture of the MODERN AMOC, which has a weaker and shallower upper cell in MODERN than in
288 modern observationally-based reconstructions (Lumpkin and Speer 2007) and state estimates, in-
289 cluding ECCO. A common procedure for reducing model drift is relaxing ocean surface values of
290 temperature and salinity to fixed climatological values (Danabasoglu et al. 2014). However, such
291 relaxation generates undesirable sources and sinks of ocean temperature and salinity that would
292 preclude an ocean state estimate that conserves those properties.

293 *b. Fitting the model to data*

294 A state estimate is considered to fit data adequately when model-data misfits normalized by ob-
295 servational errors have an approximately Gaussian distribution with mean 0 and standard deviation
296 1. By this criterion, the first-guess PRIOR simulation does not fit the MARGO data: in the annual,
297 July-August-September (JAS), and January-February-March (JFM) means, standard deviations of
298 normalized misfits are greater than 1 (Figure 4a). Moreover, the average value of normalized mis-
299 fits is less than 0, indicating a model cold bias relative to the data. Misfits exceeding observational
300 uncertainties are found in several regions. In both JAS and JFM, the model is warm relative to the
301 data in the equatorial Atlantic, the northeast Atlantic, and the western Pacific, while it is too cold
302 in the Indian, Arctic, and East Pacific Oceans (Figures 4d and 4f). In JFM, the model Southern
303 Ocean is cold relative to the data. Similarities between spatial patterns of model-data misfit and

304 MODERN-ECCO temperature anomalies suggest that model drift is a major source of error in
305 fitting the data.

306 To reduce model-data misfits, we adjust glacial atmospheric conditions and other control vari-
307 ables using the method of Lagrange multipliers (Appendix A). We found that while this approach
308 reduced misfits of both signs, it was less effective at reducing the model cold biases. To reduce
309 remaining biases after 10 iterations, we added a globally uniform increase of 2°C in all months
310 to the first guess of surface air temperatures¹. After including these changes we ran 19 additional
311 iterations, for a total of 29. An additional temperature increase of 1°C was added to the control
312 adjustments derived in January, February, and March to offset a further cold bias in that season.
313 As a reference, a separate state estimate was produced without uniform temperature adjustments;
314 the two solutions are compared in the Discussion section.

315 Changes to atmospheric control variables are typically strongest at locations coinciding with
316 MARGO gridded data, although large-scale changes show the ability of the data to influence the
317 model state in regions remote from data locations (Figure 2, right panels). Global temperature
318 increases used to reduce the model cold bias are visible in Figure 2c. Inferred changes to isopy-
319 cnal diffusivities, κ_σ , diapycnal diffusivities, κ_d , and eddy bolus velocity coefficients, κ_{GM} , are
320 small relative to their uncertainties, σ , with changes on the order of σ at few locations (Supp.
321 Figs. 1, 2, and 3). Several authors have suggested that decreased sea level at the LGM may have
322 led to increased diapycnal mixing rates in the ocean interior, as the area of shallow continen-
323 tal shelves where the bulk of tidal dissipation occurs in the modern ocean was reduced (Wunsch
324 2003; Schmittner et al. 2015). While we cannot rule out this possibility, we note that a distribution
325 of mixing parameters similar to a modern estimate suffices to fit the MARGO data, as also pointed

¹In this form of optimization, the objective function is reduced by search methods. At any stage of the search, estimates of the position of the optimized state can and should be introduced to speed convergence.

326 out by KN17. Changes to initial temperature and salinity (Supp. Figs. 4 and 5) are on the order of
327 0.01σ , as we might expect for a quasi-steady solution in which adjustments to initial conditions
328 are not important to fit the data. The important role of surface fluxes for fitting observations is
329 consistent with the dominant role of surface fluxes in the seasonal variability of the heat and salt
330 budgets in the upper ocean (Gill and Niller 1973). In contrast, changes to air-sea fluxes of heat
331 and freshwater play a dominant role in fitting the observations. We do not claim that the derived
332 control variable changes are necessary to fit the data, only that they are sufficient and reasonable
333 within their specified uncertainties.

334 Our best estimate of the glacial ocean state (GLACIAL) is the last year of a 5,000-year-long
335 MITgcm simulation run under control changes derived to fit the MARGO data. We represent the
336 state estimate by a single year rather than a time average in order to satisfy Equation 1; because
337 variability longer than a year is small, results are similar to calculations using decadal or centen-
338 nial means. The ocean state is not seasonally steady over the 5000-year integration period: for
339 instance, transience in AMOC strength is characteristic of model spin-up under adjusted bound-
340 ary conditions. However, changes in major volume transport diagnostics in the last 1000 years
341 are small relative to annual mean values (Supp. Fig. 7). Spatial patterns of MARGO-GLACIAL
342 misfits are similar to those for PRIOR but with reduced amplitudes in most regions (Figure 4,
343 right). Average model-data misfits in years 80-100 (not shown) and 4980-5000 (Figure 4a) are
344 reduced relative to PRIOR, and their normalized distribution lies close to the expected Gaussian.
345 The result satisfies the data-based criteria of Equations (2) and (3) for a quasi-seasonally-steady
346 equilibrium, and supports the conclusions of DW14 and KN17 that it is possible to fit a primitive
347 equation ocean model to the MARGO data. The fact that even our optimized physical model does
348 not exactly fit the data reflects a combination of model and data errors; these misfits are deemed

349 acceptable in light of the observational uncertainties. Subsequent adjoint iterations could likely
350 improve the model-data misfit, but at the risk of overfitting the data.

351 *c. Analysis of the state estimate*

352 We now describe properties of our best estimate of the LGM ocean state. When describing
353 abyssal properties we focus on the Atlantic Ocean, where the number of paleoceanographic data
354 is greatest.

355 1) THE UPPER OCEAN

356 Differences in the annual mean and seasonal NSSTs between GLACIAL and MODERN indi-
357 cate global cooling at the LGM except for small-amplitude warming in parts of the Arctic and
358 Southern Oceans and the Equatorial Pacific (Figure 5). The global mean NSST difference is 2°C,
359 similar to preceding estimates of $1.9 \pm 1.8^\circ\text{C}$ (MARGO), 2.2°C (KN17), and 2.4°C (in CCSM4,
360 Brady et al. 2013). The strongest cold anomalies are found in the subpolar regions, particularly
361 in the Northern Hemisphere. In addition to their data compilation, MARGO (2009) report a map
362 of LGM minus modern surface temperature anomalies based on a nearest-neighbor interpolation
363 algorithm. By comparison with their map, GLACIAL-MODERN anomalies resulting from our
364 dynamical interpolation do not show pronounced zonal gradients in the Equatorial Pacific and
365 Atlantic Oceans, while in the northern North Atlantic we find that the sign of zonal gradients is
366 reversed relative to MARGO (2009). Moreover, we find surface cooling, rather than warming, in
367 both the North Pacific and the Central Arctic. These disagreements arise because in addition to
368 fitting the data, our anomaly estimates are constrained by model physics.

369 Sea ice in GLACIAL is greater in both spatial extent and total volume than simulated in MOD-
370 ERN (Figure 6). The Arctic Ocean is filled with sea ice year-round, and winter sea ice extends

371 southward to the western coasts of Canada and Greenland and covers much of the Nordic Seas
372 and the northwest Pacific. Winter ice thicknesses in the Central Arctic are 3-5 meters, with lower
373 values in regions where ice coverage is seasonal. As in a sea ice reconstruction based on dynoflag-
374 ellate cysts (de Vernal et al. 2006), we find that GLACIAL sea ice is seasonal in the Nordic Seas
375 and northern North Atlantic. In the Southern Ocean, the spatial extent and volume of sea ice are
376 also increased in both austral summer and austral winter compared to MODERN. The 15% win-
377 ter sea ice concentration isopleth, where concentration refers to the fractional area occupied by
378 sea ice, is consistent with the maximum northward extent of sea ice reconstructed by Gersonde
379 et al. (2005), whose Southern Ocean data are included in MARGO. It also falls within the range
380 of northernmost sea ice extents simulated in PMIP3 models (Sime et al. 2016). In GLACIAL,
381 regions where brine rejection occurs due to sea ice formation coincide with the maximum winter
382 sea ice extent (SI Figure 6) in the Southern Hemisphere, and annual mean salt fluxes due to brine
383 rejection are commensurately increased (2.49×10^8 kg/s) relative to MODERN (1.57×10^8 kg/s).

384 The barotropic (vertically integrated) circulation in GLACIAL is intensified relative to MOD-
385 ERN (Figure 8), especially in the Antarctic Circumpolar Current (ACC) and subpolar gyres. Vol-
386 ume transport through the Drake Passage reaches 174 Sv (1 Sv = 10^6 m³ s⁻¹) in GLACIAL
387 compared to 117 Sv in MODERN, associated with differences in winds and increased production
388 of Antarctic Bottom Water (AABW) in GLACIAL, which can act to steepen isopycnal slopes in
389 the ACC (Gent et al. 2001; Hogg 2010). Like DW14, we find an increased southward return flow
390 in the eastern interior of the North Atlantic subtropical gyre in GLACIAL relative to MODERN,
391 though the eastward shift of the Atlantic subpolar gyre that DW14 describe is not evident. In-
392 creases in barotropic gyre circulation are consistent with increased wind stress and wind stress
393 curl.

394 Locations of deep winter mixed-layer depths (MLDs) are thought to be important for setting dis-
395 tributions of abyssal tracers because they dictate where surface water properties are communicated
396 to the abyssal interior (Gebbie and Huybers 2011; Amrhein et al. 2015) with possible implications
397 for AMOC strength (Oka et al. 2012). Comparison of maximum winter MLDs in GLACIAL and
398 MODERN reveals differences in regions of both subduction (e.g., in the model North Atlantic
399 Current) and high-latitude convection (Figure 7). In GLACIAL, reduced convection in the north-
400 east North Atlantic and Arctic Oceans is due in part to (i) reduced areas of marginal seas from
401 lower sea levels and (ii) fresher surface waters. Increased mixed layer depths in the Labrador
402 Sea are consistent with surface buoyancy losses from ocean cooling downwind of the Laurentide
403 Ice Sheet. These MLD distributions are likely affected by the model drifts discussed in Section
404 3a. However, differences between MODERN and GLACIAL, which are affected by similar drifts,
405 motivate speculation that a shift of winter maximum MLDs from the eastern to western North
406 Atlantic may contribute to differences observed in distributions of abyssal ocean tracers between
407 the LGM and today (e.g., Keigwin 2004; Curry and Oppo 2005; Marchitto and Broecker 2006)
408 because of a change in deep water source regions.

409 2) THE ABYSSAL ATLANTIC OCEAN

410 Abyssal waters in GLACIAL are everywhere colder than in MODERN in the Atlantic, where
411 zonal mean potential temperatures are reduced by roughly between 0.5 and 1.0°C (Figures 79a
412 and 9c). Increased salinity stratification (Figures 9b and 9d) is primarily responsible for greater
413 density stratification (contours, Figure 10). Higher vertical salinity stratification in the GLACIAL
414 Atlantic is consistent with larger rates of Southern Ocean brine rejection, though decreased high-
415 latitude precipitation (Figures 1g and 1h) may also play a role. GLACIAL-MODERN abyssal
416 salinity anomalies are qualitatively consistent with inferences from pore fluid reconstructions of

417 a more salinity-stratified LGM, and lie within uncertainty ranges of values derived from LGM
418 minus modern anomalies estimated from pore fluids measured at several locations in the Pacific
419 Ocean (Table 2; Insua et al. 2014). However, we do not reproduce the relatively low salinity
420 anomaly at Bermuda Rise (57.6°W , 33.7°N), or the large anomaly at Shona Rise in the Southern
421 Ocean (5.9°E , 50.0°S) that was a focus of Adkins et al. (2002). Moreover, the dispersion among
422 simulated salinity anomalies at data locations is smaller than that observed in pore fluids. Misfits
423 could be due to model biases, including inaccurate model parameterization of brine rejection, or
424 to misinterpretation of the observations (Miller et al. 2015; Wunsch 2016).

425 The upper cell of the Atlantic meridional overturning circulation (AMOC; Figures 10a and 10c)
426 is deeper and stronger in GLACIAL than MODERN by 5-10 Sv, qualitatively similar to results
427 from most PMIP3 models (Muglia and Schmittner 2015). Comparing these results to other stud-
428 ies' is complicated by errors in our state estimate due to model drift, which shoals and weakens
429 the upper cell in both MODERN and GLACIAL. Thus while our result of a relatively stronger,
430 deeper GLACIAL cell contrasts with that of KN17, who found a stronger, shallower upper LGM
431 AMOC cell, in absolute terms the LGM AMOC circulations in the two studies are similar, despite
432 differences in state estimation procedures. Our comparison of GLACIAL and MODERN also con-
433 trasts with the idealized model of Ferrari et al. (2014), who suggested that greater sea ice extent
434 at the LGM would shift outcropping isopycnals in the ACC equatorward and shoal the isopycnal
435 surface separating upper and lower AMOC cells in the Atlantic. In MODERN and GLACIAL, the
436 isopycnals dividing upper and lower cells (approximately coincident with the zero meridional flow
437 contour in Figures 10a and 10c) are the 28 and 29 kg m^{-3} potential density anomaly isopleths,
438 respectively. The deeper position of the dividing isopycnal in GLACIAL relative to MODERN is
439 accompanied by steeper ACC isopycnal slopes (Figures 10b and 10d), suggesting that the deeper,
440 stronger GLACIAL upper AMOC cell is associated with stronger ACC baroclinicity. Because

441 low-resolution models may poorly represent the role of eddies in wind-driven changes to the ACC
442 (Abernathay et al. 2011), future work should investigate these effects in an eddy-resolving ocean
443 model.

444 To test whether the GLACIAL circulation supports inference of a greater volume of southern-
445 source water in the Atlantic Ocean, we perform a dye release experiment by fixing passive tracer
446 boundary conditions in surface grid boxes to a concentration of 1 south of 60°S and to 0 elsewhere
447 in the 5000-year-long simulations of GLACIAL and MODERN. After 5000 years, the distribution
448 of this tracer in the Atlantic is very similar in the two simulations, and we conclude that fitting
449 our OGCM to the MARGO data does not require southern-source waters to shoal in the abyssal
450 Atlantic. This result further demonstrates the importance of including glacial tracer observations
451 to constrain the abyssal state.

452 4. Discussion

453 This paper presents a dynamical interpolation of seasonally-varying LGM NSST observations
454 that is approximately seasonally steady and consistent with the physics of the MITgcm. While we
455 do not claim that our glacial state estimate is a unique fit to the data, it is a dynamically plausible
456 hypothesis for LGM conditions. In agreement with simulations from climate models subject to
457 glacial climate boundary conditions and with previous glacial ocean state estimates, the upper
458 ocean at the LGM is inferred to be colder than today by 2°C in the global mean. The barotropic
459 ocean circulation is inferred to be stronger, consistent with greater wind stress and wind stress
460 curls. However, gyre circulations, while stronger, are structurally similar to the modern circulation.
461 Both perennial and seasonal sea ice extents are larger, and the central Arctic is filled with sea ice
462 year round. Regions of deep winter mixed layer depths are different from the modern. The abyssal
463 ocean is more strongly salinity stratified, with an upper AMOC cell that is stronger and deeper.

464 Our state estimate has both similarities and differences with the state estimates of DW14 and
465 KN17. For example, NSST fields reconstructed in KN17 are smoother than ours, which pre-
466 sumably reflects the isotropic 9-point (roughly 27-degree) smoothing KN17 imposed on control
467 variable adjustments. In contrast, DW14 report strong small-scale gradients in temperature be-
468 tween locations with and without LGM data, in part because they used modern oceanographic
469 conditions (rather than an estimate of glacial conditions) as a first guess. Similar to KN17, we
470 find the largest GLACIAL minus MODERN cold anomalies in the subtropics, but our estimated
471 temperature change is more uniformly negative. Like KN17, we observe a stronger salinity strat-
472 ification at the LGM, which we attribute in part to greater sea ice extent; however, while KN17
473 find a stronger, shallower AMOC, ours is stronger and deeper. These differences may stem from
474 a variety of factors, including the use of abyssal tracer observations in the KN17 solution, the
475 use of seasonal NSST observations in our solution, differences in model equilibration and spatial
476 resolution, and differences in turbulent transport parameters.

477 Because none of the solutions in DW14, KN17, and this work include error estimates, it is
478 difficult to determine whether solutions are truly in disagreement. Moreover, there is currently
479 no straightforward means to determine the range of possible solutions that can fit observations.
480 Developing tools for uncertainty quantification is an important and ongoing effort in ocean state
481 estimation (Kalmikov and Heimbach 2014). Contrasting results among LGM state estimates sug-
482 gest a sensitivity to prior choices of model controls and covariances and, more broadly, the dif-
483 ficulty in constraining the deep ocean circulation at the LGM from available observations (e.g.,
484 LeGrand and Wunsch 1995; Huybers et al. 2007; Marchal and Curry 2008; Kurahashi-Nakamura
485 et al. 2013; Gebbie et al. 2016).

486 We find that global-mean temperature changes are necessary to reduce an overall model cold
487 bias. KN17 do not find such an adjustment necessary, possibly because they used a different

488 criterion for solution convergence (KN17 evaluated how much the total cost function was reduced
489 at each adjoint iteration rather than evaluating the distribution of normalized model-data misfits) as
490 well as different choices of the first-guess ocean state and atmospheric forcings. In order to assess
491 the sensitivity of our inferences to global mean temperature changes, a separate state estimate
492 (GLACIAL_s) was computed over 6 iterations without imposing such changes. Relative to our
493 reference solution (GLACIAL), GLACIAL_s shows greater summer sea ice extent and thickness in
494 both hemispheres (Supp. Fig. 9), a stronger reduction in NSSTs (Supp. Fig. 12), colder and saltier
495 Atlantic bottom waters (Supp. Fig. 10), greater salinity and density stratification (Supp. Figs. 10
496 and 11), and a marginally stronger and shallower AMOC upper cell (Supp. Figs. 11). These
497 differences are not so large as to change our overall conclusions. To evaluate whether the mean
498 model-data misfit arises from the first guess constructed by adding CCSM4 LGM-PI anomalies
499 to modern ECCO atmospheric conditions, we ran an additional state estimate (not shown) using
500 CCSM4 LGM conditions as a first guess. We find a similar model-data bias, suggesting that
501 the first guess choice was not a major factor. A similar result (not shown) was obtained for a
502 first guess derived from a different coupled model LGM simulation (MIROC; Sueyoshi et al.
503 2013). Ultimately, the mean model-data misfit may be due to biases in the data, the MITgcm,
504 our choice of first-guess boundary conditions, the coupled models used to generate first guesses,
505 and/or the choice of boundary conditions used to force coupled models. Resolving the origin of
506 this bias is important given the use of LGM climate to infer climate sensitivity (Schmittner et al.
507 2011; Hargreaves et al. 2012) and the use of large-scale atmospheric cooling to simulate LGM
508 conditions in idealized models (Jansen 2017).

509 The GLACIAL solution is observationally consistent and approximately seasonally steady in-
510sofar as it satisfies Equations (2) and (3) and shows small drifts in transport properties relative to
511 time-mean values (Supp. Fig. 8). The fact that control adjustments derived over a relatively short

512 period (100 years) can still fit observations after a longer integration (5000 years) is not surpris-
513 ing given that the data are fit largely by local changes in surface heat fluxes, to which the upper
514 ocean adjusts on time scales shorter than 100 years; Forget et al. (2015b) found a similar result for
515 the ECCO state estimate. Adjoint integration times longer than afforded here could reveal other,
516 longer-time-scale mechanisms that also permit the ocean state to fit the data.

517 5. Perspectives

518 This work points to several ways forward to improve paleoceanographic state estimation. First,
519 there is the issue of how changes are made to atmospheric conditions in order to fit paleoceano-
520 graphic observations. In ECCO, first guess atmospheric conditions come from reanalysis products,
521 which are constrained both by satellite observations and by coupled models. The assumption in
522 ECCO is that the reanalysis products are sufficiently accurate that changes to accommodate the
523 ocean observations will have small amplitudes that are uncorrelated over large spatial scales. In
524 contrast, the first guess for pre-instrumental state estimates is poorly constrained – here, for in-
525 stance, we use the quasi-equilibrium of a free-running model (CCSM4) – and we should expect
526 that it differs from the true atmospheric state on all spatial scales, reflecting the full range of
527 coupled ocean-atmosphere dynamics. Instead, in our state estimate, we infer “patchy” control ad-
528 justments (Figure 2, right) whose length scales reflect data availability and ocean dynamics and
529 are not informed by atmospheric or coupled dynamics. While KN17 mitigated this patchiness by
530 smoothing control variables in space, it is not obvious that this approach yields more accurate at-
531 mospheric fields. A separate issue is that different choices of atmospheric controls can have similar
532 effects on the ocean state, leading to degeneracies; for instance, similarities between changes in
533 shortwave and longwave radiation inferred to fit the data (Figures 2l and 2n) reflect the inability of
534 the data and model to differentiate between different sources of ocean heating. Finally, the absence

535 of feedbacks between the ocean and atmosphere in the presence of large changes to atmospheric
536 forcings can lead to unphysical patterns of heating and cooling that contribute to model drift.
537 These caveats urge caution in attempting to rationalize inferred atmospheric conditions physically
538 and point to a need for coupled ocean-ice-atmosphere state estimation.

539 Second, assuming a steady or seasonally steady LGM ocean circulation at once provides a strong
540 constraint on the state estimate – possibly as strong as that provided by the data – and poses
541 technical challenges for reaching model equilibrium. In this work, we found that long simulations
542 intended to equilibrate the deep ocean to reconstructed surface conditions led to strong model
543 drifts. An alternative approach could be to include patterns and timescales of temperature and
544 salinity relaxation, which can reduce model drift, in the control vector for purposes of constructing
545 a state estimate. Once the estimation procedure has converged, it may be possible to reinterpret
546 fluxes due to relaxation in terms of atmospheric fluxes. More broadly, the extent to which the
547 ocean circulation is ever in equilibrium (including at the LGM) is unclear. Paleoceanographic data
548 provide an important arena for challenging assumptions about climate stationarity, and steadiness
549 should only be assumed when absolutely necessary. Satisfying a version of Equations (2) and (3)
550 yields a solution that is only as steady as the data require and provides a less restrictive modeling
551 criterion for the steadiness of the LGM and other geologic intervals.

552 Third, this work raises the question of how well suited the current generation of ocean mod-
553 els is to paleoceanographic state estimation, particularly for abyssal properties. Unlike in the
554 modern state estimation problem, there are no direct measurements of ocean hydrography at the
555 LGM. While the MARGO data can constrain some features in the surface ocean, the impact of
556 surface temperature data on inferences of abyssal properties is mediated by deep-water formation
557 processes that are typically parameterized and that occur in poorly sampled regions such as the
558 Antarctic shelf and Labrador Sea. Locations and rates of high-latitude deep water formation are

559 important for setting abyssal values of temperature, salinity, and passive tracers (Amrhein et al.
560 2015). We expect that improving model representations of high-latitude processes will be effective
561 at increasing the accuracy of reconstructed abyssal ocean conditions at the LGM.

562 Finally, LGM state estimation will benefit from an increased number, spatial coverage, and
563 diversity of proxy observations, as well as greater understanding of how to represent those obser-
564 vations in numerical models. Of particular utility is the inclusion of abyssal tracer measurements,
565 which inspire many hypotheses about LGM watermass reorganizations. While KN17 take the im-
566 portant step of including carbon and oxygen stable isotope measurements in their state estimation,
567 realizing the full potential of these measurements is challenging because of the long time scales of
568 tracer equilibration (Wunsch and Heimbach 2008), which necessitates running long and computa-
569 tionally expensive adjoint simulations. Dail (2012), Amrhein (2016), and KN17 describe technical
570 improvements on this front that should be explored in future work. Ultimately, the goal is to derive
571 a state estimate using all possible observations from the LGM and to include new observations as
572 they become available.

573 *Acknowledgments.* The authors acknowledge Patrick Heimbach, Raffaele Ferrari, Mick Follows,
574 and David McGee for helpful comments on an earlier version of the work, as well as thoughtful
575 comments from three reviewers that improved the manuscript. An Nguyen, Jeff Scott, and Jean-
576 Michel Campin provided important assistance with the MITgcm adjoint. Computing time was
577 provided by NASA Advanced Supercomputing and Ames Research Center. DEA was supported
578 by a NSF Graduate Research Fellowship and NSF grant OCE-1060735. OM acknowledges sup-
579 port from the NSF. GF was supported by NASA award #1553749 and Simons Fundation award
580 #549931. The adjoint model was generated using TAF (Giering and Kaminski 1998). Output from
581 the state estimate is available by contacting the corresponding author.

APPENDIX

583 **Seasonal state estimation by the method of least squares with Lagrange multipliers**

584 Seasonal state estimation seeks to minimizes a scalar cost function $J(\underline{\mathbf{u}})$ to find a set of controls,
 585 $\underline{\mathbf{u}}$, such that the model monthly mean values satisfy Equations (1)-(3). In this work, $J(\underline{\mathbf{u}})$ is the
 586 sum of three contributions. The first contribution, J_{data} is the squared, weighted model-data misfit,
 587 which itself has three terms,

$$\begin{aligned} J_{data} &= \frac{1}{L^{Ann}} \sum_{i=1}^{L^{Ann}} \left(\mathbf{y}_i^{Ann} - \mathbf{E}^{Ann} \underline{\mathbf{x}} \right)^\top \left(\underline{\mathbf{R}}^{Ann} \right)^{-1} \left(\mathbf{y}_i^{Ann} - \mathbf{E}^{Ann} \underline{\mathbf{x}} \right) \\ &\quad + \frac{1}{3L^{JFM}} \sum_{i=1}^{L^{JFM}} \left(\mathbf{y}_i^{JFM} - \mathbf{E}^{JFM} \underline{\mathbf{x}} \right)^\top \left(\underline{\mathbf{R}}^{JFM} \right)^{-1} \left(\mathbf{y}_i^{JFM} - \mathbf{E}^{JFM} \underline{\mathbf{x}} \right) \\ &\quad + \frac{1}{3L^{JAS}} \sum_{i=1}^{L^{JAS}} \left(\mathbf{y}_i^{JAS} - \mathbf{E}^{JAS} \underline{\mathbf{x}} \right)^\top \left(\underline{\mathbf{R}}^{JAS} \right)^{-1} \left(\mathbf{y}_i^{JAS} - \mathbf{E}^{JAS} \underline{\mathbf{x}} \right), \end{aligned} \quad (\text{A1})$$

588 where the L are numbers of observations available in each time period (annual, JFM, and JAS);
 589 \mathbf{y}_i^{Ann} , \mathbf{y}_i^{JFM} and \mathbf{y}_i^{JAS} are observations; the matrices $\underline{\mathbf{R}}^{Ann}$, $\underline{\mathbf{R}}^{JAS}$, and $\underline{\mathbf{R}}^{JFM}$ have the form of $\underline{\mathbf{R}} =$
 590 $\langle \underline{\mathbf{n}} \underline{\mathbf{n}}^\top \rangle$, where angle brackets denote the expected value, and are the observational noise covariance
 591 constructed from MARGO uncertainty estimates; and the matrices \mathbf{E}^{Ann} , \mathbf{E}^{JAS} , and \mathbf{E}^{JFM} relate
 592 model variables across space and time to the data. Multiplication by 1/3 for JFM and JAS divides
 593 by the number of model monthly means included in the cost function; for annual observations, this
 594 factor is 1. The second contribution,

$$J_{model} = -2 \sum_{m=0}^{M-1} \mu(t)^\top [\mathbf{x}(t) - \mathcal{L}(\mathbf{x}(t - \Delta t), \mathbf{q}(t - \Delta t), \underline{\mathbf{u}})], \quad t = m\Delta t, \quad (\text{A2})$$

595 where $\mu(t)$ is a vector of Lagrange multipliers that serves to impose the MITgcm model equations
 596 upon the solution. The vector $\underline{\mathbf{u}}$ can more generally represent model errors as well. The last
 597 contribution,

$$J_{ctrl} = \underline{\mathbf{u}}^\top \mathbf{Q}^{-1} \underline{\mathbf{u}}, \quad (\text{A3})$$

598 penalizes control adjustments, where \mathbf{Q} is the error covariance of the control variables. Here \mathbf{Q}
599 is assumed to be zero except for diagonal values that are equal to the squared standard deviations
600 (σ) assumed for control variable uncertainties (Table 1).

601 Minimization of the total cost function, $J = J_{data} + J_{ctrl} + J_{model}$, is a problem of constrained
602 nonlinear optimization, whereby model-data misfit is reduced through a choice of control variables
603 and the state vector evolution obeys the dynamical constraints in Equation (1). The dimension
604 of the state vector and the complexity of \mathcal{L} preclude an analytical solution. Instead, automatic
605 differentiation of the MITgcm code (Giering and Kaminski 1998) is used to adjust the control
606 variables iteratively in the direction of locally steepest descent using a quasi-Newton algorithm
607 (Gilbert and Lemaréchal 1989). After each iteration, the cost function and local sensitivities are
608 recomputed and the procedure is repeated until the distribution of model-data misfits, normalized
609 by observational uncertainty, approximates a normal (Gaussian) distribution with zero mean and
610 unity variance. At this point, the state estimate is considered acceptable, so long as the control
611 adjustments are also acceptable. For a more detailed discussion see Wunsch and Heimbach (2007).

612 References

- 613 Abernathey, R., J. Marshall, and D. Ferreira, 2011: The dependence of Southern Ocean meridional
614 overturning on wind stress. *Journal of Physical Oceanography*, **41** (12), 2261–2278.
- 615 Adcroft, A., C. Hill, J.-M. Campin, J. Marshall, and P. Heimbach, 2004: Overview of the formu-
616 lation and numerics of the MIT GCM. *Proceedings of the ECMWF seminar series on Numeri-*
617 *cal Methods, Recent developments in numerical methods for atmosphere and ocean modelling,*
618 139–149.

- 619 Adkins, J. F., K. McIntyre, and D. P. Schrag, 2002: The salinity, temperature, and $\delta^{18}\text{O}$ of the
620 glacial deep ocean. *Science*, **298 (5599)**, 1769–1773.
- 621 Alkama, R., M. Kageyama, and G. Ramstein, 2006: Freshwater discharges in a simulation of
622 the Last Glacial Maximum climate using improved river routing. *Geophysical research letters*,
623 **33 (21)**.
- 624 Amrhein, D. E., 2016: Inferring Ocean Circulation during the Last Glacial Maximum and Last
625 Deglaciation Using Data and Models. Ph.D. thesis, MIT-WHOI Joint Program.
- 626 Amrhein, D. E., G. Gebbie, O. Marchal, and C. Wunsch, 2015: Inferring surface water equilibrium
627 calcite $\delta^{18}\text{O}$ during the last deglacial period from benthic foraminiferal records: Implications
628 for ocean circulation. *Paleoceanography*.
- 629 Braconnot, P., and Coauthors, 2007: Results of PMIP2 coupled simulations of the Mid-Holocene
630 and Last Glacial Maximum—Part 1: experiments and large-scale features.
- 631 Brady, E. C., B. L. Otto-Bliesner, J. E. Kay, and N. Rosenbloom, 2013: Sensitivity to glacial
632 forcing in the CCSM4. *Journal of Climate*, **26 (6)**, 1901–1925.
- 633 Brovkin, V., A. Ganopolski, D. Archer, and S. Rahmstorf, 2007: Lowering of glacial atmospheric
634 CO₂ in response to changes in oceanic circulation and marine biogeochemistry. *Paleoceanog-*
635 *raphy*, **22 (4)**.
- 636 Bryan, K., 1984: Accelerating the convergence to equilibrium of ocean-climate models. *Journal*
637 *of Physical Oceanography*, **14 (4)**, 666–673.
- 638 Bugnion, V., and C. Hill, 2006: Equilibration mechanisms in an adjoint ocean general circulation
639 model. *Ocean Dynamics*, **56 (1)**, 51–61.

- 640 Burke, A., O. Marchal, L. I. Bradtmiller, J. F. McManus, and R. François, 2011: Application of
641 an inverse method to interpret $^{231}\text{Pa}/^{230}\text{Th}$ observations from marine sediments. *Paleoceanog-*
642 *raphy*, **26** (1).
- 643 Clark, P., and Coauthors, 2012: Global climate evolution during the last deglaciation. *Proceedings*
644 *of the National Academy of Sciences*, **109** (19), E1134–E1142.
- 645 Curry, W., J. Duplessy, L. Labeyrie, and N. Shackleton, 1988: Changes in the distribution of d13C
646 of deep water sigmaCO₂ between the last glaciation and the Holocene. *Paleoceanography*, **3** (3),
647 317–341.
- 648 Curry, W., and D. Oppo, 2005: Glacial water mass geometry and the distribution of $\delta^{13}\text{C}$ of ΣCO_2
649 in the western Atlantic Ocean. *Paleoceanography*, **20** (1), PA1017.
- 650 Dail, H., 2012: Atlantic Ocean circulation at the Last Glacial Maximum: Inferences from data and
651 models. Ph.D. thesis, MIT-WHOI Joint Program.
- 652 Dail, H., and C. Wunsch, 2014: Dynamical Reconstruction of Upper-Ocean Conditions in the Last
653 Glacial Maximum Atlantic. *Journal of Climate*, **27** (2), 807–823.
- 654 Danabasoglu, G., and Coauthors, 2014: North Atlantic simdanabasoglu2014northulations in coor-
655 dinated ocean-ice reference experiments phase II (CORE-II). Part I: mean states. *Ocean Mod-*
656 *elling*, **73**, 76–107.
- 657 de Vernal, A., A. Rosell-Melé, M. Kucera, C. Hillaire-Marcel, F. Eynaud, M. Weinelt, T. Dokken,
658 and M. Kageyama, 2006: Comparing proxies for the reconstruction of LGM sea-surface condi-
659 tions in the northern North Atlantic. *Quaternary Science Reviews*, **25** (21), 2820–2834.

- 660 Duplessy, J., N. Shackleton, R. Fairbanks, L. Labeyrie, D. Oppo, and N. Kallel, 1988: Deepwa-
661 ter source variations during the last climatic cycle and their impact on the global deepwater
662 circulation. *Paleoceanography*, **3** (3), 343–360.
- 663 Fekete, B. M., C. J. Vörösmarty, and W. Grabs, 2002: High-resolution fields of global runoff com-
664 bining observed river discharge and simulated water balances. *Global Biogeochemical Cycles*,
665 **16** (3).
- 666 Ferrari, R., M. F. Jansen, J. F. Adkins, A. Burke, A. L. Stewart, and A. F. Thompson, 2014:
667 Antarctic sea ice control on ocean circulation in present and glacial climates. *Proceedings of the*
668 *National Academy of Sciences*, **111** (24), 8753–8758.
- 669 Forget, G., J.-M. Campin, P. Heimbach, C. Hill, R. Ponte, and C. Wunsch, 2015a: ECCO version
670 4: an integrated framework for non-linear inverse modeling and global ocean state estimation.
- 671 Forget, G., D. Ferreira, and X. Liang, 2015b: On the observability of turbulent transport rates by
672 Argo: supporting evidence from an inversion experiment. *Ocean Science*, **11** (5), 839.
- 673 Gaspar, P., Y. Grégoris, and J.-M. Lefevre, 1990: A simple eddy kinetic energy model for simula-
674 tions of the oceanic vertical mixing: Tests at station Papa and Long-Term Upper Ocean Study
675 site. *Journal of Geophysical Research: Oceans*, **95** (C9), 16 179–16 193.
- 676 Gebbie, G., 2014: How much did Glacial North Atlantic Water shoal? *Paleoceanography*, **29** (3),
677 190–209.
- 678 Gebbie, G., and P. Huybers, 2006: Meridional circulation during the Last Glacial Maximum ex-
679 plored through a combination of South Atlantic $\delta^{18}\text{O}$ observations and a geostrophic inverse
680 model. *Geochemistry Geophysics Geosystems*, **7** (11), Q11N07.

- 681 Gebbie, G., and P. Huybers, 2011: How is the ocean filled? *Geophysical Research Letters*, **38** (6),
682 L06 604.
- 683 Gebbie, G., G. J. Streletz, and H. J. Spero, 2016: How well would modern-day oceanic property
684 distributions be known with paleoceanographic-like observations? *Paleoceanography*.
- 685 Gent, P. R., W. G. Large, and F. O. Bryan, 2001: What sets the mean transport through Drake
686 Passage? *Journal of Geophysical Research: Oceans*, **106** (C2), 2693–2712.
- 687 Gent, P. R., and J. C. McWilliams, 1990: Isopycnal mixing in ocean circulation models. *Journal*
688 *of Physical Oceanography*, **20** (1), 150–155.
- 689 Gent, P. R., and Coauthors, 2011: The community climate system model version 4. *Journal of*
690 *Climate*, **24** (19), 4973–4991.
- 691 Gersonde, R., X. Crosta, A. Abelmann, and L. Armand, 2005: Sea-surface temperature and sea ice
692 distribution of the Southern Ocean at the EPILOG Last Glacial Maximum—a circum-Antarctic
693 view based on siliceous microfossil records. *Quaternary Science Reviews*, **24** (7), 869–896.
- 694 Giering, R., and T. Kaminski, 1998: Recipes for adjoint code construction. *ACM Transactions on*
695 *Mathematical Software (TOMS)*, **24** (4), 437–474.
- 696 Gilbert, J. C., and C. Lemaréchal, 1989: Some numerical experiments with variable-storage quasi-
697 Newton algorithms. *Mathematical programming*, **45** (1-3), 407–435.
- 698 Gill, A., and P. Niller, 1973: The theory of the seasonal variability in the ocean. *Deep Sea Research*
699 *and Oceanographic Abstracts*, Elsevier, Vol. 20, 141–177.
- 700 Griffies, S. M., and Coauthors, 2009: Coordinated Ocean-ice Reference Experiments (COREs).
701 *Ocean Modelling*, **26** (1-2), 1–46, doi:10.1016/j.ocemod.2008.08.007, URL <http://dx.doi.org/10.1016/j.ocemod.2008.08.007>, arXiv:1011.1669v3.

- 703 Guilyardi, E., 2006: El Niño–mean state–seasonal cycle interactions in a multi-model ensemble.
- 704 *Climate Dynamics*, **26** (4), 329–348.
- 705 Hargreaves, J., A. Paul, R. Ohgaito, A. Abe-Ouchi, and J. Annan, 2011: Are paleoclimate model
- 706 ensembles consistent with the MARGO data synthesis? *Climate of the Past*, **7** (3), 917–933.
- 707 Hargreaves, J. C., J. D. Annan, M. Yoshimori, and A. Abe-Ouchi, 2012: Can the Last Glacial
- 708 Maximum constrain climate sensitivity? *Geophysical Research Letters*, **39** (24).
- 709 Hogg, A. M., 2010: An Antarctic Circumpolar Current driven by surface buoyancy forcing. *Geo-*
- 710 *physical Research Letters*, **37** (23).
- 711 Huybers, P., G. Gebbie, and O. Marchal, 2007: Can paleoceanographic tracers constrain merid-
- 712 ional circulation rates? *Journal of physical oceanography*, **37** (2), 394–407.
- 713 Insua, T. L., A. J. Spivack, D. Graham, S. D'Hondt, and K. Moran, 2014: Reconstruction of Pacific
- 714 Ocean bottom water salinity during the Last Glacial Maximum. *Geophysical Research Letters*,
- 715 **41** (8), 2914–2920.
- 716 Jansen, M. F., 2017: Glacial ocean circulation and stratification explained by reduced atmospheric
- 717 temperature. *Proceedings of the National Academy of Sciences*, **114** (1), 45–50.
- 718 Jansen, M. F., and L.-P. Nadeau, 2016: The Effect of Southern Ocean Surface Buoyancy Loss
- 719 on the Deep-Ocean Circulation and Stratification. *Journal of Physical Oceanography*, **46** (11),
- 720 3455–3470.
- 721 Kalmikov, A. G., and P. Heimbach, 2014: A Hessian-based method for uncertainty quantification
- 722 in global ocean state estimation. *SIAM Journal on Scientific Computing*, **36** (5), S267–S295.
- 723 Kara, A. B., P. A. Rochford, and H. E. Hurlbert, 2000: An optimal definition for ocean mixed
- 724 layer depth. Tech. rep., DTIC Document.

- 725 Keigwin, L. D., 2004: Radiocarbon and stable isotope constraints on Last Glacial Maximum and
726 Younger Dryas ventilation in the western North Atlantic. *Paleoceanography*, **19** (4).
- 727 Kurahashi-Nakamura, T., M. Losch, and A. Paul, 2013: Can sparse proxy data constrain the
728 strength of the Atlantic meridional overturning circulation? *Geoscientific Model Development
729 Discussions*, **6** (3), 4417–4445.
- 730 Kurahashi-Nakamura, T., A. Paul, and M. Losch, 2017: Dynamical reconstruction of the global
731 ocean state during the Last Glacial Maximum. *Paleoceanography*, **32** (4), 326–350.
- 732 Large, W. G., and S. G. Yeager, 2004: *Diurnal to decadal global forcing for ocean and sea-
733 ice models: the data sets and flux climatologies*. National Center for Atmospheric Research
734 Boulder.
- 735 LeGrand, P., and C. Wunsch, 1995: Constraints from paleotracer data on the North Atlantic circu-
736 lation during the last glacial maximum. *Paleoceanography*, **10** (6), 1011–1045.
- 737 Losch, M., D. Menemenlis, J.-M. Campin, P. Heimbach, and C. Hill, 2010: On the formulation
738 of sea-ice models. Part 1: Effects of different solver implementations and parameterizations.
739 *Ocean Modelling*, **33** (1), 129–144.
- 740 Lumpkin, R., and K. Speer, 2007: Global ocean meridional overturning. *Journal of Physical
741 Oceanography*, **37** (10), 2550–2562.
- 742 Lynch-Stieglitz, J., and Coauthors, 2007: Atlantic meridional overturning circulation during the
743 Last Glacial Maximum. *science*, **316** (5821), 66–69.
- 744 Marchal, O., and W. B. Curry, 2008: On the abyssal circulation in the glacial Atlantic. *Journal of
745 Physical Oceanography*, **38** (9), 2014–2037.

- 746 Marchitto, T. M., and W. S. Broecker, 2006: Deep water mass geometry in the glacial Atlantic
747 Ocean: A review of constraints from the paleonutrient proxy Cd/Ca. *Geochemistry, Geophysics,
748 Geosystems*, **7** (12).
- 749 Marchitto, T. M., D. W. Oppo, and W. B. Curry, 2002: Paired benthic foraminiferal Cd/Ca and
750 Zn/Ca evidence for a greatly increased presence of Southern Ocean Water in the glacial North
751 Atlantic. *Paleoceanography*, **17** (3), 10–1.
- 752 MARGO Project Members, 2009: Constraints on the magnitude and patterns of ocean cooling at
753 the Last Glacial Maximum. *Nature Geoscience*, **2** (2), 127–132.
- 754 Marshall, J., A. Adcroft, C. Hill, L. Perelman, and C. Heisey, 1997: A finite-volume, incompress-
755 ible Navier Stokes model for studies of the ocean on parallel computers. *Journal of Geophysical
756 Research: Oceans (1978–2012)*, **102** (C3), 5753–5766.
- 757 Marzocchi, A., and M. F. Jansen, 2017: Connecting Antarctic sea ice to deep-ocean circulation in
758 modern and glacial climate simulations. *Geophysical Research Letters*, **44** (12), 6286–6295.
- 759 McIntyre, A., N. G. Kipp, A. W. Bé, T. Crowley, T. Kellogg, J. V. Gardner, W. Prell, and W. F. Rud-
760 diman, 1976: Glacial North Atlantic 18,000 years ago: a CLIMAP reconstruction. *Geological
761 Society of America Memoirs*, **145**, 43–76.
- 762 Miller, M. D., M. Simons, J. F. Adkins, and S. E. Minson, 2015: The Information Content of Pore
763 Fluid δ 18O and [Cl-]. *Journal of Physical Oceanography*, **45** (8), 2070–2094.
- 764 Mix, A. C., E. Bard, and R. Schneider, 2001: Environmental processes of the ice age: land, oceans,
765 glaciers (EPILOG). *Quaternary Science Reviews*, **20** (4), 627–657.
- 766 Muglia, J., and A. Schmittner, 2015: Glacial Atlantic overturning increased by wind stress in
767 climate models. *Geophysical Research Letters*, **42** (22), 9862–9868.

- 768 Oka, A., H. Hasumi, and A. Abe-Ouchi, 2012: The thermal threshold of the Atlantic meridional
769 overturning circulation and its control by wind stress forcing during glacial climate. *Geophysical*
770 *Research Letters*, **39** (9), 0–1.
- 771 Otto-Bliesner, B., C. Hewitt, T. Marchitto, E. Brady, A. Abe-Ouchi, M. Crucifix, S. Murakami,
772 and S. Weber, 2007: Last Glacial Maximum ocean thermohaline circulation: PMIP2 model
773 intercomparisons and data constraints. *Geophysical Research Letters*, **34** (12).
- 774 Otto-Bliesner, B. L., and Coauthors, 2009: A comparison of PMIP2 model simulations and the
775 MARGO proxy reconstruction for tropical sea surface temperatures at last glacial maximum.
776 *Climate Dynamics*, **32** (6), 799–815.
- 777 Peltier, W., 2004: Global glacial isostasy and the surface of the ice-age Earth: The ICE-5G (VM2)
778 model and GRACE. *Annu. Rev. Earth Planet. Sci.*, **32**, 111–149.
- 779 Pflaumann, U., and Coauthors, 2003: Glacial North Atlantic: Sea-surface conditions reconstructed
780 by GLAMAP 2000. *Paleoceanography*, **18** (3).
- 781 Redi, M. H., 1982: Oceanic isopycnal mixing by coordinate rotation. *Journal of Physical*
782 *Oceanography*, **12** (10), 1154–1158.
- 783 Sarmiento, J., and J. Toggweiler, 1984: A new model for the role of the oceans in determining
784 atmospheric pCO₂. *Nature*, **308** (5960), 621–624.
- 785 Schmittner, A., J. Green, and S.-B. Wilmes, 2015: Glacial ocean overturning intensified by tidal
786 mixing in a global circulation model. *Geophysical Research Letters*, **42** (10), 4014–4022.
- 787 Schmittner, A., N. M. Urban, J. D. Shakun, N. M. Mahowald, P. U. Clark, P. J. Bartlein, A. C.
788 Mix, and A. Rosell-Melé, 2011: Climate sensitivity estimated from temperature reconstructions
789 of the Last Glacial Maximum. *Science*, **334** (6061), 1385–1388.

- 790 Shakun, J., and Coauthors, 2012: Global warming preceded by increasing carbon dioxide concen-
791 trations during the last deglaciation. *Nature*, **484** (7392), 49–54.
- 792 Siegenthaler, U., and T. Wenk, 1984: Rapid atmospheric CO₂ variations and ocean circulation.
793 *Nature*, **308** (5960), 624–626.
- 794 Sime, L. C., D. Hodgson, T. J. Bracegirdle, C. Allen, B. Perren, S. Roberts, and A. M. de Boer,
795 2016: Sea ice led to poleward-shifted winds at the Last Glacial Maximum: the influence of state
796 dependency on CMIP5 and PMIP3 models. *Climate of the Past*, **12** (12), 2241.
- 797 Smith, W. H., and D. T. Sandwell, 1997: Global sea floor topography from satellite altimetry and
798 ship depth soundings. *Science*, **277** (5334), 1956–1962.
- 799 Stammer, D., and Coauthors, 2002: Global ocean circulation during 1992–1997, estimated from
800 ocean observations and a general circulation model. *Journal of Geophysical Research: Oceans*,
801 **107** (C9).
- 802 Sueyoshi, T., and Coauthors, 2013: Set-up of the PMIP3 paleoclimate experiments conducted
803 using an Earth system model, MIROC-ESM. *Geoscientific Model Development*, **6** (3), 819–836.
- 804 Tao, W., L. Yi, and H. Wei, 2013: Last glacial maximum sea surface temperatures: A model-data
805 comparison. *Atmospheric and Oceanic Science Letters*, **6** (5), 233–239.
- 806 Winguth, A., D. Archer, E. Maier-Reimer, and U. Mikolajewicz, 2000: Paleonutrient data analysis
807 of the glacial Atlantic using an adjoint ocean general circulation model. *Inverse Methods in*
808 *Global Biogeochemical Cycles. Geophys. Monogr.*, **114**, 171–183.
- 809 Wunsch, C., 2003: Determining paleoceanographic circulations, with emphasis on the Last Glacial
810 Maximum. *Quaternary Science Reviews*, **22** (2), 371–385.

- 811 Wunsch, C., 2006: *Discrete inverse and state estimation problems: with geophysical fluid appli-*
812 *cations*. Cambridge Univ Pr.
- 813 Wunsch, C., 2016: Last Glacial Maximum and deglacial abyssal seawater oxygen isotopic ratios.
814 *Climate of the Past*, **12** (6), 1281–1296.
- 815 Wunsch, C., and P. Heimbach, 2007: Practical global oceanic state estimation. *Physica D: Non-*
816 *linear Phenomena*, **230** (1), 197–208.
- 817 Wunsch, C., and P. Heimbach, 2008: How long to oceanic tracer and proxy equilibrium? *Quater-*
818 *nary Science Reviews*, **27** (7-8), 637–651.
- 819 Zhang, X., G. Lohmann, G. Knorr, and X. Xu, 2013: Different ocean states and transient charac-
820 *teristics in Last Glacial Maximum simulations and implications for deglaciation. Climate of the*
821 *Past*, **9**, 2319–2333.

822 LIST OF TABLES

823	Table 1. Control variables, control uncertainty standard deviations (σ), sources of first-	
824	guess control values, and time periods for control variables used in the LGM	
825	state estimate. ECCO refers to the ECCO version 4 release 2 simulation in	
826	the year 2007. Δ CCSM4 refers to LGM minus pre-industrial control runs in	
827	coupled CCSM4 simulations (Figure 2). κ_σ , κ_d , and κ_{GM} refer to coefficients	
828	of isopycnal diffusivity (Redi 1982), diapycnal diffusivity, and eddy diffusivity	
829	associated with the bolus velocity (Gent and McWilliams 1990). “PRIOR”	
830	refers to the forward simulation under ECCO + Δ CCSM4 forcings described in	
831	Section 2d.	40
832	Table 2. Comparison of LGM-Holocene bottom water salinities from pore fluid mea-	
833	surements and model results from this study. Pore fluid measurements were	
834	not included in the cost function and thus provide an independent assessment	
835	of the LGM state estimate. Salinity differences $S_{GLACIAL} - S_{MODERN}$ are from	
836	the deepest grid box at the model grid location nearest core sites. All values are	
837	on the practical salinity scale.	41

Control variable	σ	Units	Source of first guess	Time period
SW radiation	20	Wm^{-2}	ECCO+ ΔCCSM4	Monthly mean
LW radiation	20	Wm^{-2}	ECCO+ ΔCCSM4	Monthly mean
Specific humidity	2×10^{-3}	–	ECCO+ ΔCCSM4	Monthly mean
Precipitation	4×10^{-8}	ms^{-1}	ECCO+ ΔCCSM4	Monthly mean
2m air temperature	4	K	ECCO+ ΔCCSM4	Monthly mean
Zonal wind stress	0.1	Pa	ECCO+ ΔCCSM4	Monthly mean
Meridional wind stress	0.1	Pa	ECCO+ ΔCCSM4	Monthly mean
κ_d	10^{-4}	m^2s^{-1}	ECCO	Constant
κ_σ	500	m^2s^{-1}	ECCO	Constant
κ_{GM}	500	m^2s^{-1}	ECCO	Constant
Initial temperature	3	K	PRIOR	Initial condition
Initial salinity	1	–	PRIOR	Initial condition

TABLE 1: Control variables, control uncertainty standard deviations (σ), sources of first-guess control values, and time periods for control variables used in the LGM state estimate. ECCO refers to the ECCO version 4 release 2 simulation in the year 2007. ΔCCSM4 refers to LGM minus pre-industrial control runs in coupled CCSM4 simulations (Figure 2). κ_σ , κ_d , and κ_{GM} refer to coefficients of isopycnal diffusivity (Redi 1982), diapycnal diffusivity, and eddy diffusivity associated with the bolus velocity (Gent and McWilliams 1990). “PRIOR” refers to the forward simulation under ECCO + ΔCCSM4 forcings described in Section 2d.

Latitude	Longitude	Depth (m)	$S_{GLACIAL} - S_{ModCtrl}$	Pore fluid ΔS	Reference
33.7°N	57.6°W	4584	1.40	0.95±0.03	Adkins et al. (2002)
55.5°N	14.7°W	2184	1.07	1.16±0.11	Adkins et al. (2002)
41.8°S	171.5°W	3290	1.31	1.46±0.08	Adkins et al. (2002)
50.0°S	5.9°E	3626	1.32	2.40±0.17	Adkins et al. (2002)
30.4°N	157.9°W	5813	1.31	1.37± 0.18	Insua et al. (2014)
20.7°N	143.4°W	5412	1.31	1.51± 0.18	Insua et al. (2014)
2.8°N	110.6°W	3760	1.26	1.38± 0.09	Insua et al. (2014)
23.9°S	165.6°W	5695	1.33	1.55± 0.09	Insua et al. (2014)
41.9°S	153.1°W	5074	1.32	1.20± 0.09	Insua et al. (2014)

TABLE 2: Comparison of LGM-Holocene bottom water salinities from pore fluid measurements and model results from this study. Pore fluid measurements were not included in the cost function and thus provide an independent assessment of the LGM state estimate. Salinity differences $S_{GLACIAL} - S_{MODERN}$ are from the deepest grid box at the model grid location nearest core sites. All values are on the practical salinity scale.

838 LIST OF FIGURES

839	Fig. 1. Flowchart describing the construction of simulated ocean states (MODERN and PRIOR) 840 and data-constrained glacial state estimates (GLACIAL and GLACIAL_s) described in this 841 manuscript. We use 5000-year-long simulations to equilibrate the MITgcm to different sets 842 of model control variables (or “controls:” atmospheric conditions, turbulent transport pa- 843 rameters, and initial conditions). MODERN (Section 3a) gives a model representation of 844 modern oceanographic conditions; PRIOR is a first-guess glacial state that is the starting 845 point for LGM state estimation (Section 2d); GLACIAL is the LGM state estimate that is 846 the main result of this paper; and GLACIAL_s is used to diagnose sensitivity of the state 847 estimate to uniform adjustments in surface air temperature (see Discussion). Modern initial 848 conditions used for MODERN and PRIOR are taken from the ECCO v4 state estimate (For- 849 get et al. 2015a) from the year 2007; an additional 1.1 salinity is added to every grid box 850 in PRIOR based on the global mean salinity change estimated at the LGM by Adkins et al. 851 (2002).	44
852	Fig. 2. Left: LGM minus pre-industrial annual-mean anomalies of atmospheric variables in 853 CCSM4 (Brady et al. 2013). Right: Adjustments to atmospheric control variables (annual 854 means) derived to fit the MITgcm to MARGO data. Panel (f) includes a uniform change in 855 global mean temperature made to fit the data.	45
856	Fig. 2. (continued)	46
857	Fig. 3. Annual mean deviations of surface salinity and temperature in GLACIAL and MODERN 858 from modern properties are illustrated by comparing to the ECCO state estimate. “Sur- 859 face” is here taken to mean the uppermost model gridbox, which is centered on 5 m wa- 860 ter depth. MODERN surface temperatures show basin-scale deviations from ECCO (a). 861 A similar pattern is seen in GLACIAL-ECCO temperature anomalies (c), in addition to 862 an overall cooling. GLACIAL-ECCO salinity anomalies on the practical salinity scale (d) 863 have been corrected by subtracting 1.1 to account for the mean salinity increase imposed in 864 GLACIAL. Similarities between GLACIAL-ECCO and MODERN-ECCO anomalies sug- 865 gest that model drift affects GLACIAL and MODERN similarly, motivating the choice of 866 MODERN as a basis for computing LGM-modern anomalies.	47
867	Fig. 4. Model-data misfits of NSSTs are improved in the state estimation procedure. (a) Histograms 868 of model-data misfits for annual-, JFM-, and JAS-mean values in PRIOR and GLACIAL 869 normalized by data uncertainties. GLACIAL misfits are similar to a standard normal Gaus- 870 sian distribution (grey), indicating an acceptable fit to the data. (b)-(g) Model-data misfits 871 normalized by data uncertainties for PRIOR (left) and GLACIAL (right) annual-, JFM-, and 872 JAS-mean data (rows 1, 2, and 3, respectively). Blue (red) values indicate that the model is 873 cold (warm) relative to the data. GLACIAL shows similar patterns of misfits as PRIOR, but 874 with reduced amplitudes of both signs.	48
875	Fig. 5. GLACIAL minus MODERN temperature anomalies in the uppermost grid box centered on 876 5 m water depth during (a) the annual mean, (b) January-February-March mean, and (c) 877 July-August-September mean.	49
878	Fig. 6. Sea ice thickness in GLACIAL (colors) and 15% concentration isopleth in September (left) 879 and March (right) of both hemispheres for MODERN (gray contour) and GLACIAL (black 880 contour).	50
881	Fig. 7. Annual mean mixed layer depth computed using the MLD criterion of Kara et al. (2000) for 882 MODERN (top) and GLACIAL (bottom) in March (left) and September (right).	51

883	Fig. 8. Barotropic (vertically integrated) streamfunction in GLACIAL (left) and the GLACIAL-	
884	MODERN barotropic streamfunction anomaly (right). Barotropic transport in the Antarctic	
885	Circumpolar Current in GLACIAL exceeds that of MODERN by more than 100 Sv in places	
886	($1 \text{ Sv} = 10^6 \text{ m}^3 \text{ s}^{-1}$).	52
887	Fig. 9. Atlantic zonal mean potential temperature (left) and salinity (right, on the practical salinity	
888	scale) in MODERN (top) and GLACIAL (bottom).	53
889	Fig. 10. Atlantic (left) and global (right) zonal mean meridional overturning streamfunctions in	
890	MODERN (top) and GLACIAL (bottom). Contours denote potential density in kg/m^3 minus	
891	a reference value of 1000 kg/m^3 . Note differences in colorbars between global and Atlantic	
892	overturning and non-constant potential density contour intervals. Potential density differ-	
893	ences between LGM and GLACIAL reflect in part a global mean salinity increase of 1.1 in	
894	GLACIAL.	54
895	Fig. 11. Concentrations at model year 5000 of a passive tracer held at a surface value of 1 south of	
896	60°S and 0 elsewhere in MODERN (left) and GLACIAL (right).	55

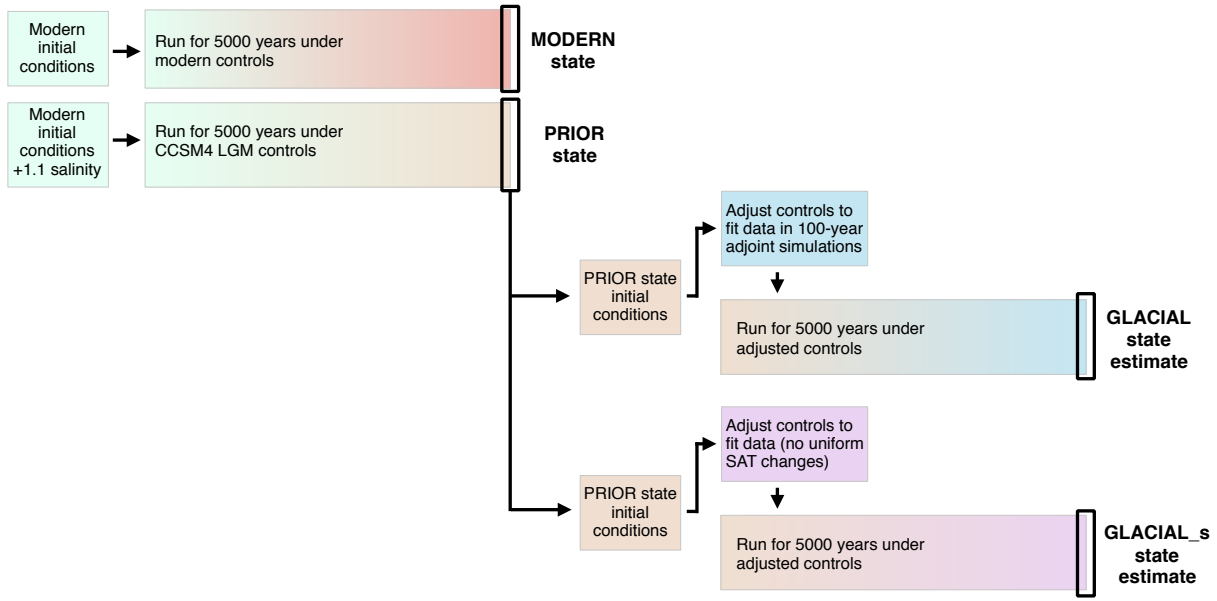


FIG. 1: Flowchart describing the construction of simulated ocean states (MODERN and PRIOR) and data-constrained glacial state estimates (GLACIAL and GLACIAL_s) described in this manuscript. We use 5000-year-long simulations to equilibrate the MITgcm to different sets of model control variables (or “controls:” atmospheric conditions, turbulent transport parameters, and initial conditions). MODERN (Section 3a) gives a model representation of modern oceanographic conditions; PRIOR is a first-guess glacial state that is the starting point for LGM state estimation (Section 2d); GLACIAL is the LGM state estimate that is the main result of this paper; and GLACIAL_s is used to diagnose sensitivity of the state estimate to uniform adjustments in surface air temperature (see Discussion). Modern initial conditions used for MODERN and PRIOR are taken from the ECCO v4 state estimate (Forget et al. 2015a) from the year 2007; an additional 1.1 salinity is added to every grid box in PRIOR based on the global mean salinity change estimated at the LGM by Adkins et al. (2002).

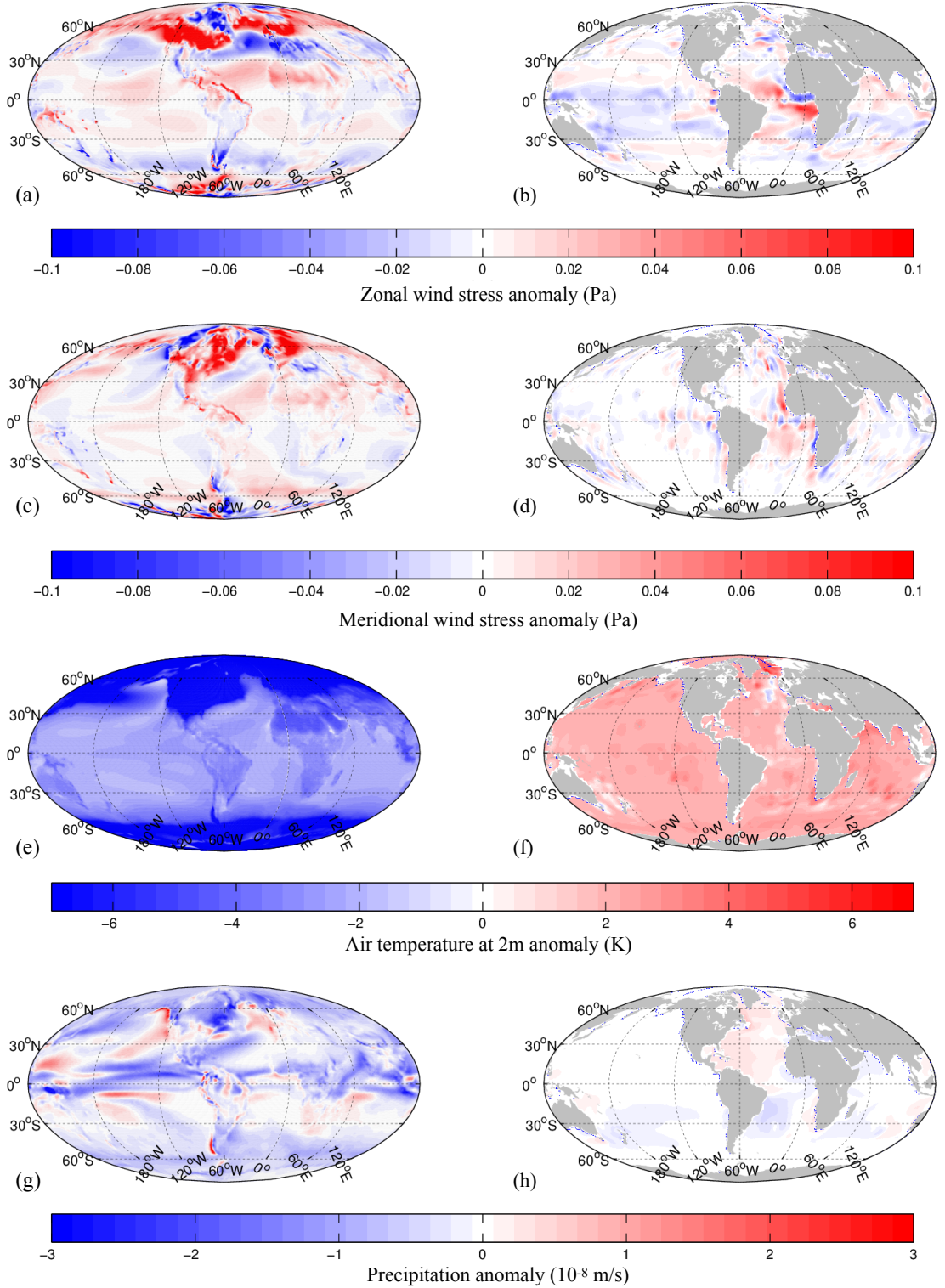


FIG. 2: Left: LGM minus pre-industrial annual-mean anomalies of atmospheric variables in CCSM4 (Brady et al. 2013). Right: Adjustments to atmospheric control variables (annual means) derived to fit the MITgcm to MARGO data. Panel (f) includes a uniform change in global mean temperature made to fit the data.

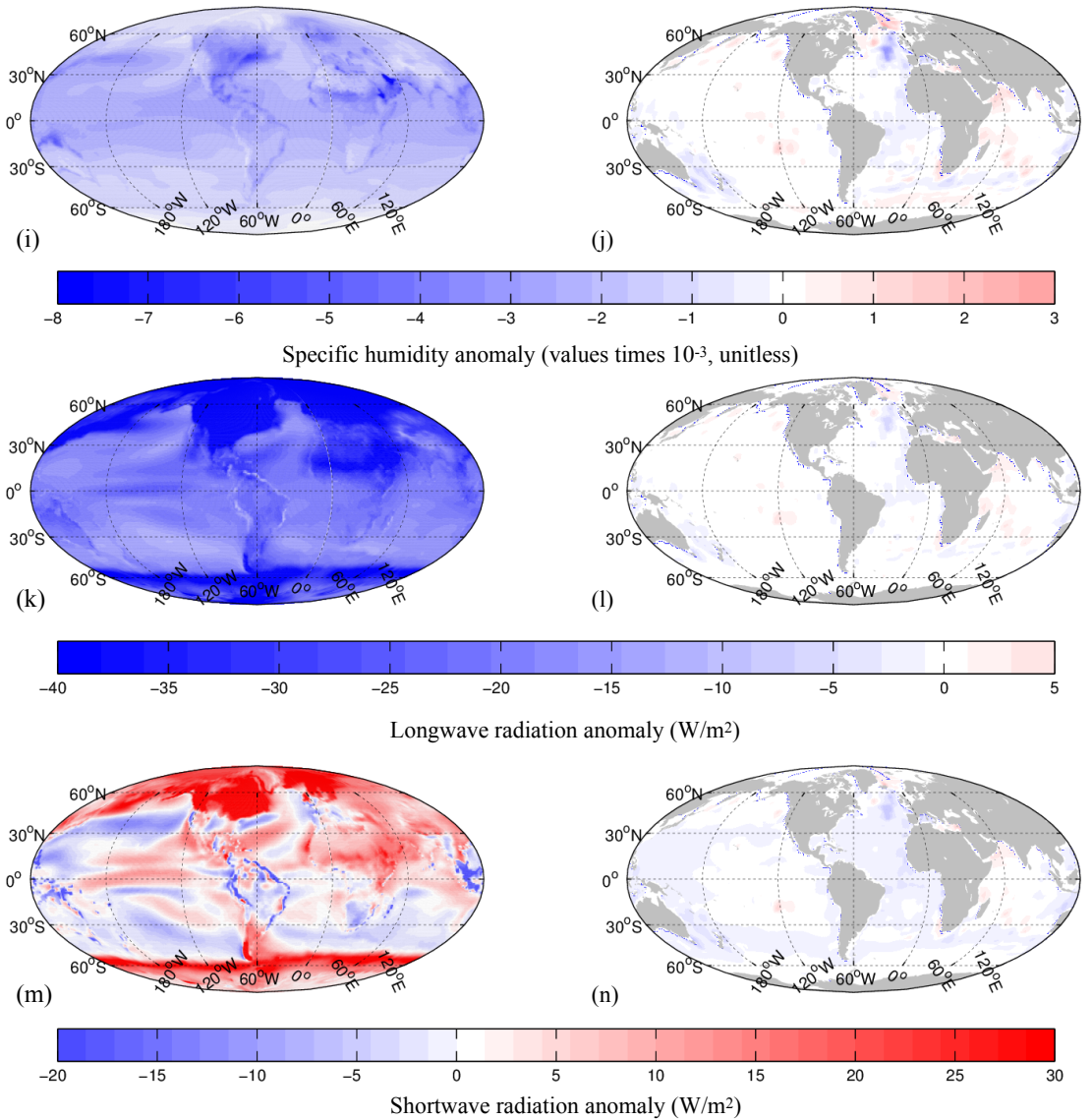


FIG. 2: (continued)

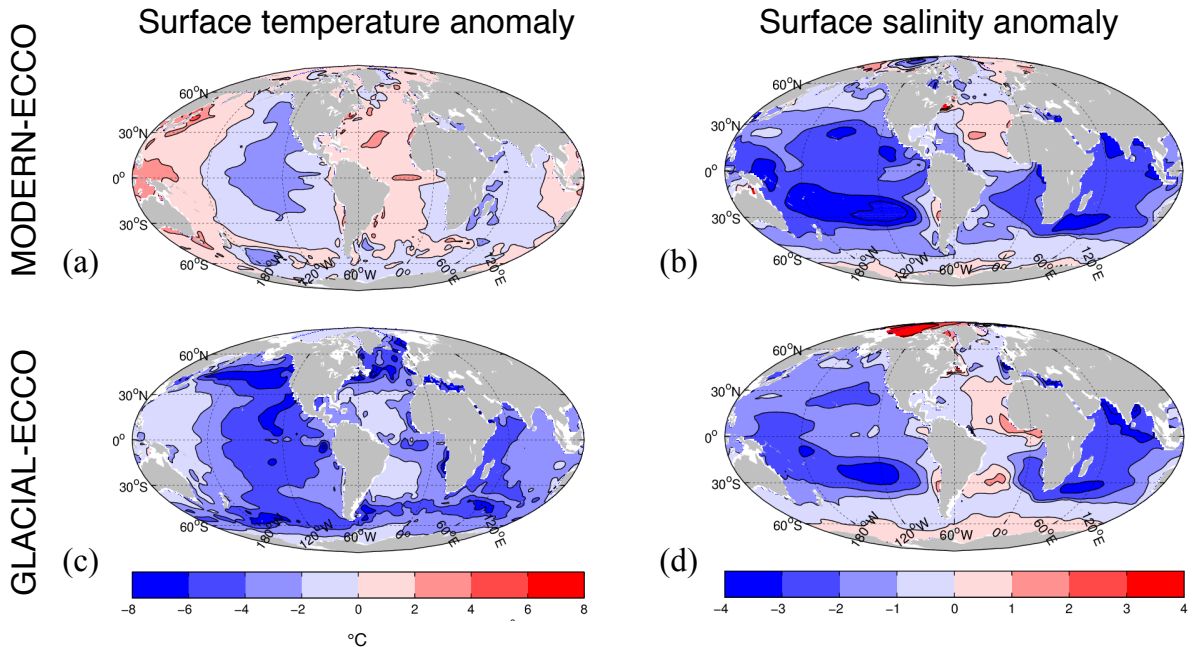


FIG. 3: Annual mean deviations of surface salinity and temperature in GLACIAL and MODERN from modern properties are illustrated by comparing to the ECCO state estimate. “Surface” is here taken to mean the uppermost model gridbox, which is centered on 5 m water depth. MODERN surface temperatures show basin-scale deviations from ECCO (a). A similar pattern is seen in GLACIAL-ECCO temperature anomalies (c), in addition to an overall cooling. GLACIAL-ECCO salinity anomalies on the practical salinity scale (d) have been corrected by subtracting 1.1 to account for the mean salinity increase imposed in GLACIAL. Similarities between GLACIAL-ECCO and MODERN-ECCO anomalies suggest that model drift affects GLACIAL and MODERN similarly, motivating the choice of MODERN as a basis for computing LGM-modern anomalies.

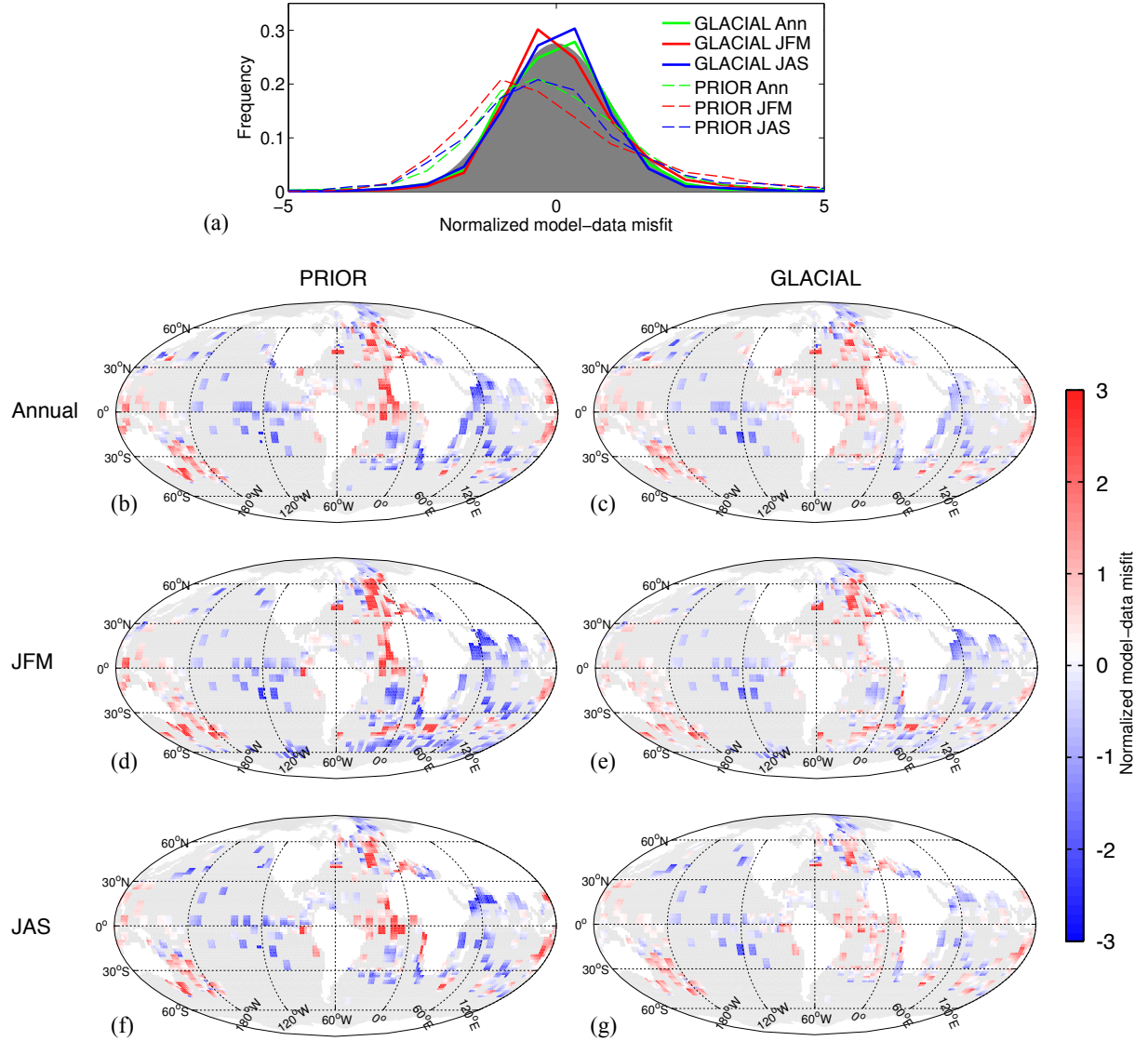


FIG. 4: Model-data misfits of NSSTs are improved in the state estimation procedure. (a) Histograms of model-data misfits for annual-, JFM-, and JAS-mean values in PRIOR and GLACIAL normalized by data uncertainties. GLACIAL misfits are similar to a standard normal Gaussian distribution (grey), indicating an acceptable fit to the data. (b)-(g) Model-data misfits normalized by data uncertainties for PRIOR (left) and GLACIAL (right) annual-, JFM-, and JAS-mean data (rows 1, 2, and 3, respectively). Blue (red) values indicate that the model is cold (warm) relative to the data. GLACIAL shows similar patterns of misfits as PRIOR, but with reduced amplitudes of both signs.

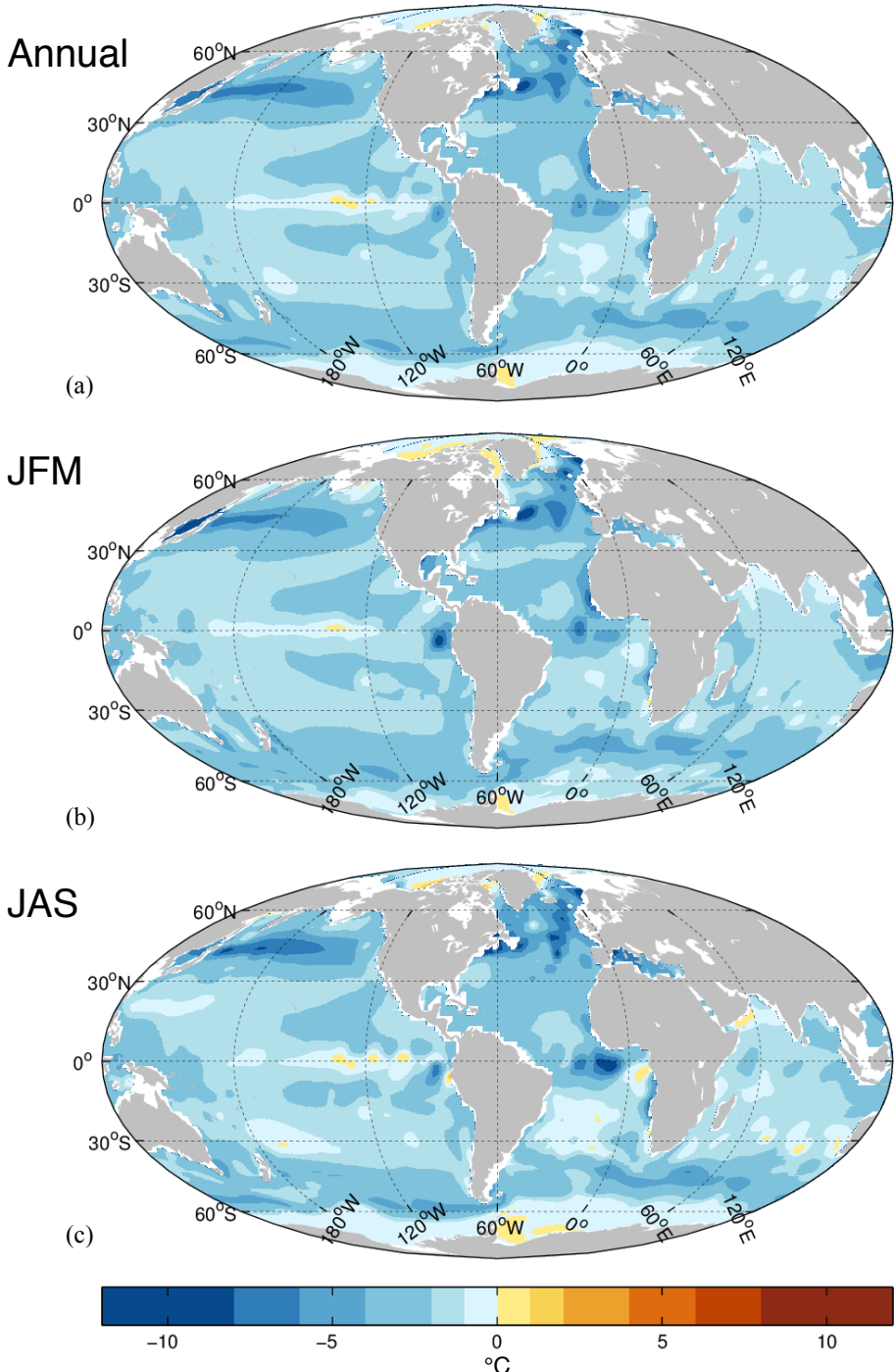


FIG. 5: GLACIAL minus MODERN temperature anomalies in the uppermost grid box centered on 5 m water depth during (a) the annual mean, (b) January–February–March mean, and (c) July–August–September mean.

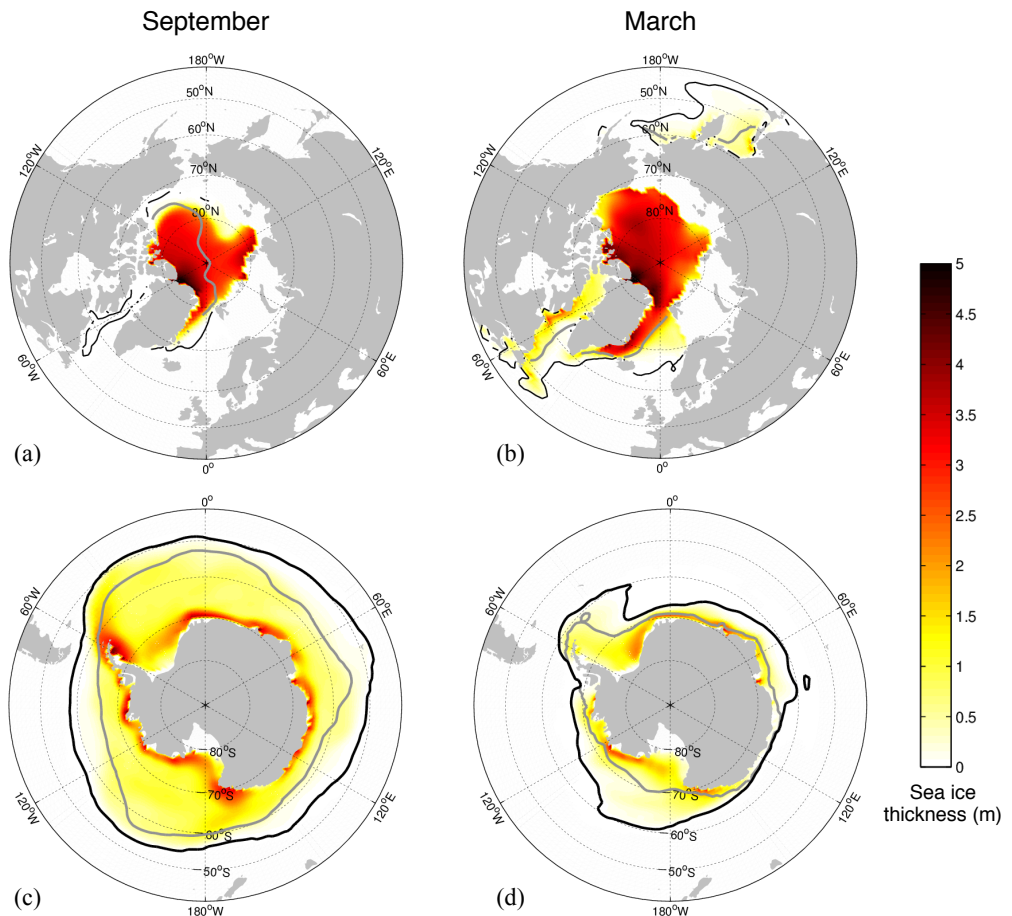


FIG. 6: Sea ice thickness in GLACIAL (colors) and 15% concentration isopleth in September (left) and March (right) of both hemispheres for MODERN (gray contour) and GLACIAL (black contour).

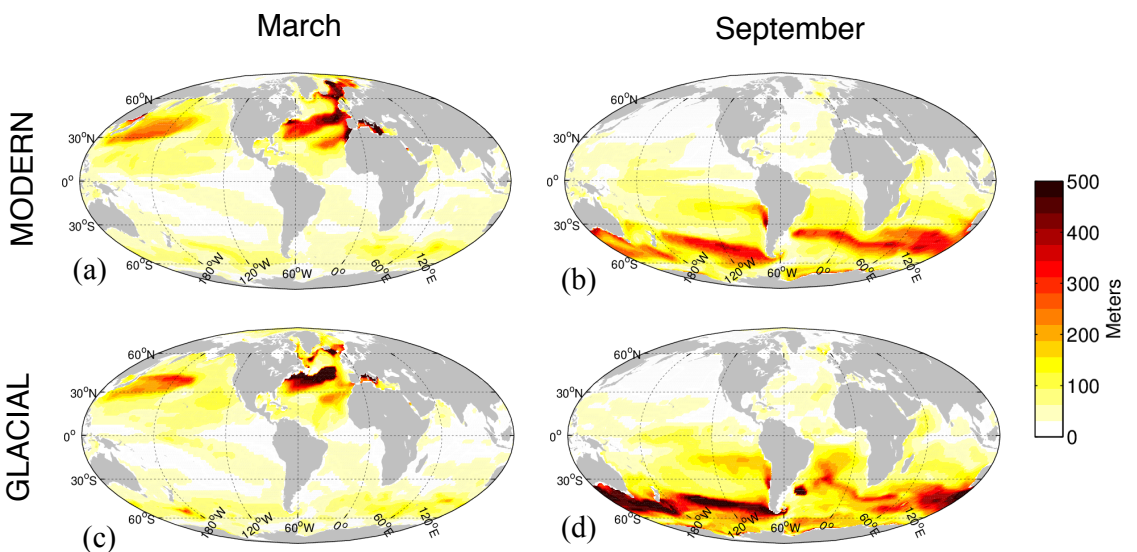


FIG. 7: Annual mean mixed layer depth computed using the MLD criterion of Kara et al. (2000) for MODERN (top) and GLACIAL (bottom) in March (left) and September (right).

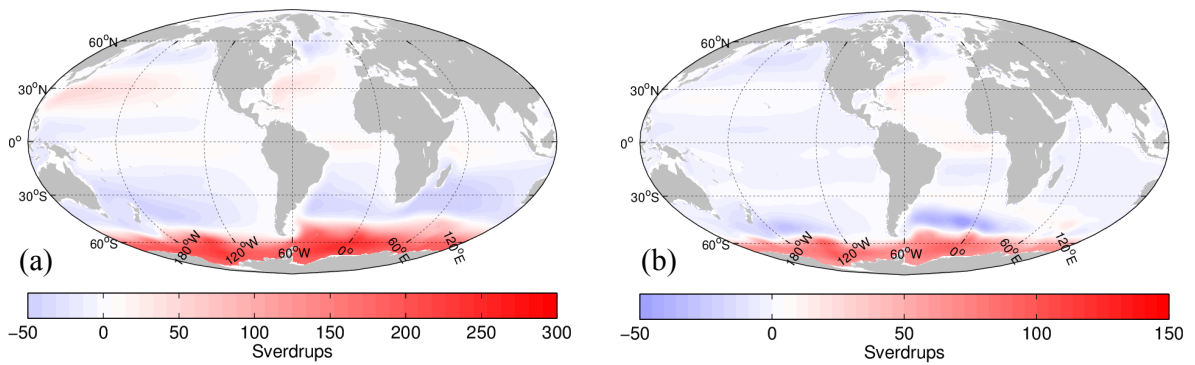


FIG. 8: Barotropic (vertically integrated) streamfunction in GLACIAL (left) and the GLACIAL-MODERN barotropic streamfunction anomaly (right). Barotropic transport in the Antarctic Circumpolar Current in GLACIAL exceeds that of MODERN by more than 100 Sv in places ($1 \text{ Sv} = 10^6 \text{ m}^3 \text{ s}^{-1}$).

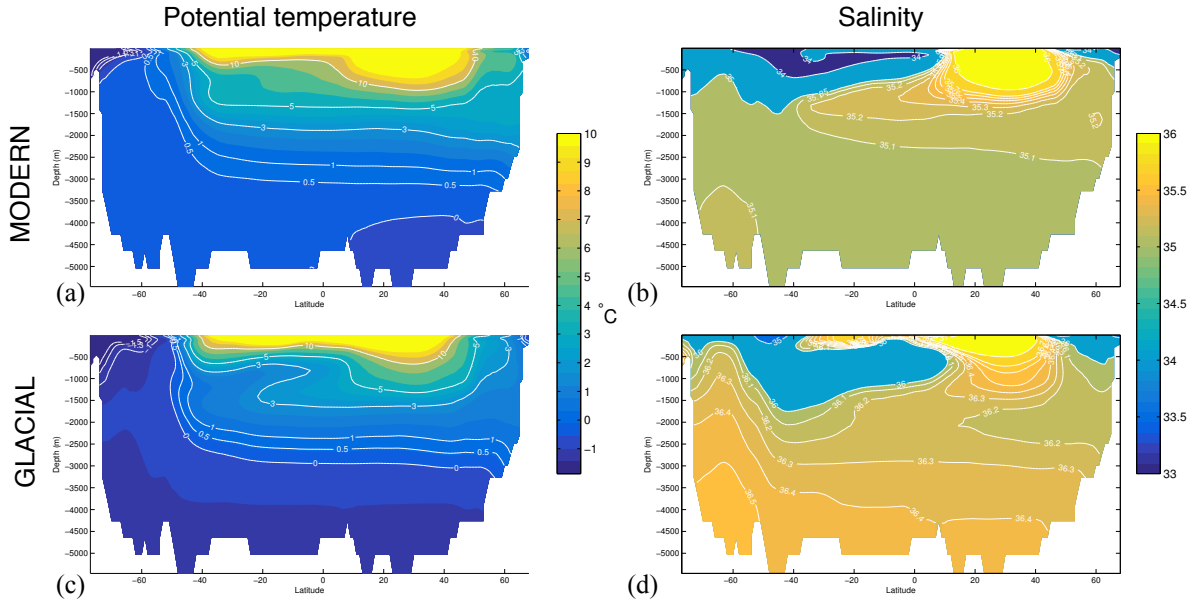


FIG. 9: Atlantic zonal mean potential temperature (left) and salinity (right, on the practical salinity scale) in MODERN (top) and GLACIAL (bottom).

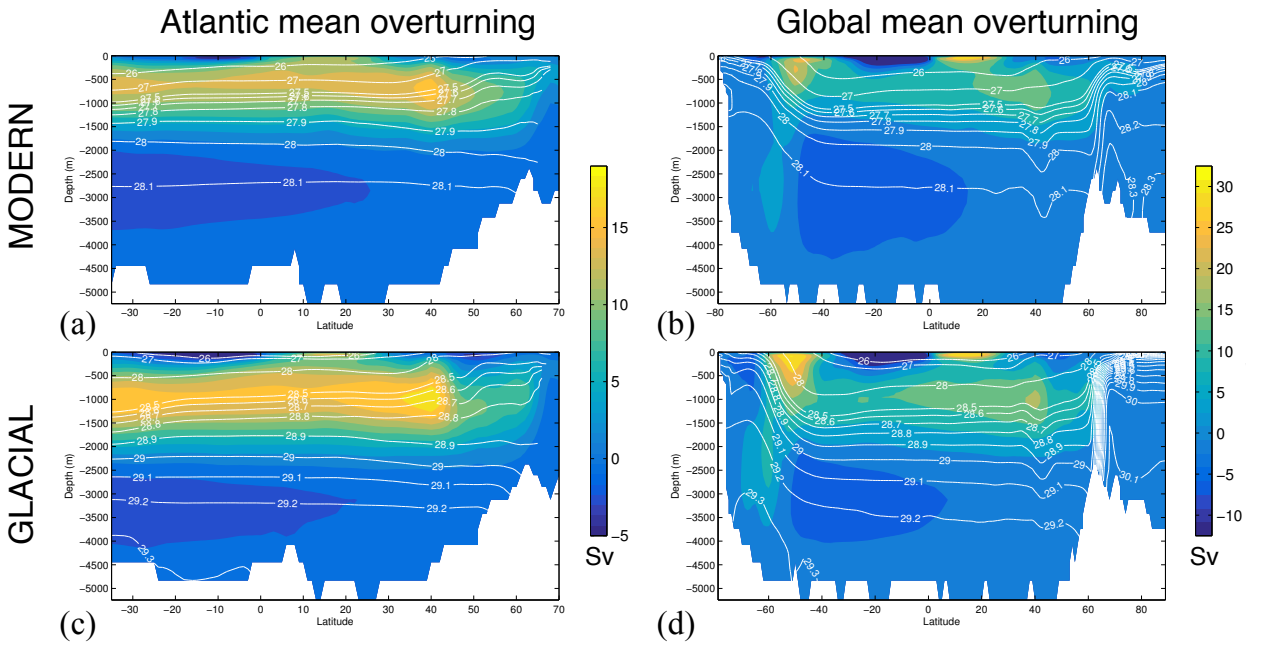


FIG. 10: Atlantic (left) and global (right) zonal mean meridional overturning streamfunctions in MODERN (top) and GLACIAL (bottom). Contours denote potential density in kg/m^3 minus a reference value of 1000 kg/m^3 . Note differences in colorbars between global and Atlantic overturning and non-constant potential density contour intervals. Potential density differences between LGM and GLACIAL reflect in part a global mean salinity increase of 1.1 in GLACIAL.

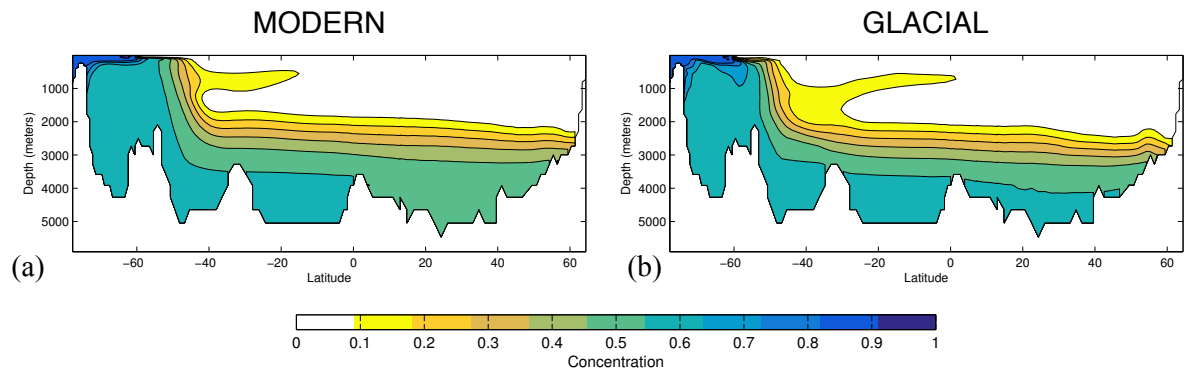


FIG. 11: Concentrations at model year 5000 of a passive tracer held at a surface value of 1 south of 60° S and 0 elsewhere in MODERN (left) and GLACIAL (right).